Polarization Dependent Ablation of Diamond with Gaussian and Orbital Angular Momentum Laser Beams

Maryam Alameer

Thesis submitted to the Faculty of Graduate and Postdoctoral Studies

In partial fulfilment of the requirements For

the M.Sc. degree in Physics

Physics

Faculty of Science

University of Ottawa

I would like to dedicate this thesis to my loving parents and husband . . .

Acknowledgements

I want to thank my supervisor professor Ravi Bhardwaj for the great and valuable knowledge that he has shared and contributed with the project team members during my research. I also would like to thank my colleagues for the continuous cooperation and assistance. Furthermore, I would like to thank my parents and my husband for their unlimited support and motivation during my studies journey.

Abstract

The vectorial nature (polarization) of light plays a significant role in light-matter interaction that leads to a variety of optical devices. The polarization property of light has been exploited in imaging, metrology, data storage, optical communication and also extended to biological studies. Most of the past studies fully explored and dealt with the conventional polarization state of light that has spatially symmetric electrical field geometry such as linear and circular polarization. Recently, researchers have been attracted to light whose electric field vector varies in space, the so-called optical vector vortex beam (VVB). Such light is expected to further enhance and improve the efficiency of optical systems. For instance, a radially polarized light under focusing condition is capable of a tighter focus more than the general optical beams with a uniform polarization structure, which improves the resolution of the imaging system [1].

Interaction of ultrafast laser pulses with matter leads to numerous applications in material processing and biology for imaging and generation of microfluidic systems. A femtosecond pulse, with very high intensities of $(10^{12} - 10^{13}\ W/cm^2)$, has the potential to trigger a phenomenon of optical breakdown at the surface and therefore induce permanent material modification. With such high intensities and taking into account the fact that most materials possess large bandgap, the interaction is completely nonlinear in nature, and the target material can be modified locally upon

the surface and even further in bulk. The phenomenon of optical breakdown can be further investigated by studying the nonlinear absorption. Properties like very short pulse duration and the high irradiance of ultrashort laser pulse lead to more precise results during the laser ablation process over the long pulsed laser. The duration of femtosecond laser pulse provides a high resolution for material processing because of the significant low heat-affected zone (HAZ) beyond the desired interaction spot generated upon irradiating the material. Under certain condition, the interaction of intense ultrashort light pulses with the material gives rise to the generation of periodic surface structures with a sub-micron periodicity, i.e., much smaller than the laser wavelength. The self-oriented periodic surface structures generated by irradiating the material with multiple femtosecond laser pulses results in improving the functionality of the material's surface such as controlling wettability, improving thin film adhesion, and minimizing friction losses in automobile engines, consequently, influences positively on many implementations.

In this work, we introduced a new method to study complex polarization states of light by imprinting them on a solid surface in the form of periodic nano-structures. Micro/Nanostructuring of diamond by ultrafast pulses is of extreme importance because of its potential applications in photonics and other related fields. We investigated periodic surface structures usually known as laser-induced periodic surface structures (LIPSS) formed by Gaussian beam as well as with structured light carrying orbital angular momentum (OAM), generated by a birefringent optical device called a q-plate (QP). We generated conventional nano-structures on diamond surface using linearly and circularly polarized Gaussian lights at different number of pulses and variable pulse energies. In addition, imprinting the complex polarization state of different orders of optical vector vortex beams on a solid surface was fulfilled in the form of periodic structures oriented parallel to the local electric field of optical light. We also produced a variety of unconventional surface structures by

superimposing a Gaussian beam with a vector vortex beam or by superposition of different order vector vortex beams.

This thesis is divided into five chapters, giving a brief description about laser-matter interaction, underlying the unique characterization of femtosecond laser over the longer pulse laser and mechanisms of material ablation under the irradiation of fs laser pulse. This chapter also presents some earlier studies reported in formation of (LIPSS) fabricated on diamond with Gaussian. The second chapter explains the properties of twisted light possessing orbital angular momentum in its wavefront, a few techniques used for OAM generation including a full explanation of the q-plate from the fabrication to the function of the q-plate, and the tool utilized to represent the polarization state of light (SoP), a Poincaré sphere. Finally, the experimental details and results are discussed in the third and fourth chapters, respectively, following with a conclusion chapter that briefly summarizes the thesis and some potential application of our findings.

Contents

List of Figures

List of Tables

Chapter 1

Introduction

1.1 Motivation

Beyond jewelry, diamond has surpassed many minerals such as silicon, gallium nitride and silicon carbide in several technological applications due to its remarkable optical, chemical and mechanical properties. Properties such as wide bandgap (5.47 eV), broad transmission spectrum extended from 220 nm up to $>$ 50 μm [2], high refractive index of 2.4 at 800 nm, high thermal conductivity $>$ 2000 W/mK and extreme hardness and rigidity stands it out from other materials in various advanced applications. For example, photodetectors, high power electronic devices [3], electrochemical detectors and cutting tools.

Besides its unique features, diamond possesses other exceptional aspects such as color centers. Color centers are a type of crystallographic defect in which one or more unpaired electrons occupy the anionic vacancy in a crystal lattice. Electrons in such a vacancy tend to absorb light in the visible spectrum such that the materials that are usually transparent become colored. Color centers are not just an approach to coloration in diamond crystal, but also considered as an ideal platform for data

processing due to its long-lived spin quantum states (atom-like properties) [4].

The most common defect found and regenerated in diamond is nitrogen-vacancies (N-V), where its photo-luminescence property has been exploited in various novel applications such as quantum computing and spintronics [4]. It was found that N-V center in chemical vapor deposition (CVD) single crystal diamond has long coherent time for electron spin reaches to 58 μs at 300 K [5]. Also, because the accessibility of sensing, reading and manipulation of the spin state at the N-V center, the N-V defect has performed a promising candidate for new applications in quantum information processing.

In general, the conventional method to form lattice vacancies in diamond is by bombarding the diamond with high energy particles, and then annealing it at extremely high temperatures. For example, the N-V vacancy consists of lattice vacancies generated by irradiation with nitrogen ions, and these formed vacancies at room temperature are generally inactive. Thus, annealing at an extremely high temperature between 600°C and 800°C is required to move vacancies closer to the nitrogen in order to create the nitrogen-vacancies. Unlike the extreme environment involved in the conventional method and its high cost, there is an efficient technique [6] which does not involve extreme conditions to generate N-V center that succeeds over the old method. It exploits the capability of femtosecond laser in enhancing color center formation through wave-guide fabrication in diamond.

Furthermore, the use of femtosecond laser writing technique has been significantly increased to create laser-induced periodic surface structures (LIPSS) that have a periodicity of sub-wavelength width and usually known as nano-ripples. LIPSS are fabricated at relatively high laser energy and can also be used as sampling cells [7], fluidic channels [8] and interferometers [9]. Machining of micrometer scale surfaces at low and high fluence regimes, via femtosecond laser direct writ-

ing technologies, are used to fabricate micro-devices such as fiber optics [10]. Such nano-ripples enhance the material's optical, mechanical and chemical properties for applications of material surface in various researches. It is worth noting that the properties of such LIPSS can be used for controlling the properties of water repellence [11], diffuse reflection [12], and surface friction [13]. Also, due to nanoscale structures generated on gold by multipulse femtosecond laser ablation, the absorptance of gold was enhanced by a factor of about 3 [14]. At sufficiently high fluence with a large number of incident pulses, the material can exhibit almost complete absorption of light [14].

Moreover, because of the remarkable properties of OAM beams like offering an extra degree of freedom for photon, it motivated researchers to exploit, explore and study the properties of a physical system under the effect of such beams. Our motivation was an attempt to generate complex, unconventional nano-surface structures on single crystal diamond through femtosecond laser writing method. Following, it also led to accurate imprinting of the polarization state of light onto the diamond surface. We have been able to investigate the nano-ripples structures formed upon the irradiation of Gaussian and optical vortex beams on diamond's surface. Also, understating of femtosecond laser-matter interaction gained through our results and findings can be further developed for improving micromachining strategies in ultrafast laser processing of materials. As for example, with detailed knowledge of the light-matter interaction, controlling the experimental parameters, had enabled the researchers to extend the micromachining techniques from labs to industry [15]. We also extended to map complex asymmetrical states of polarization (SoPs) generated from superpositions of different order optical vortex beams.

1.2 Femtosecond laser-matter interaction

1.2.1 Nonlinear absorption and ionization

- **Multiphoton and tunnelling ionization**

  According to Einstein's photoelectric effect, emission of electrons or other free-carriers occurs when photon energy is equal or higher than the work function of the material. This is known as a linear absorption process where a single photon can move the valance electron to the conduction band as shown in figure 1.1. Accordingly, if the photon energies are less than the material bandgap then linear absorption process cannot induce such transitions [16, 17]. Inter-band transmissions are still possible with low energy photons provided several of them can participate in a cumulative process. In other words, multiple femtosecond pulses are needed to excite the electrons from the valance to the conduction band as shown in figure 1.1. The energy of m-photons incident on the material must exceed the energy bandgap of the target material according to the following relationship:

$$m\hbar\omega \geq E_g, \tag{1.1}$$

  where E_g is the material bandgap, $\hbar$ is the reduced Planck constant and ω is the laser frequency. Such a process is called nonlinear ionization/excitation and requires very large photon flux vis-a-vis intensities. For example, diamond sample has an optical bandgap of 5.47 eV. To fulfil the relationship (1.1), four photons injection process (a photon with an energy of approximately 1.57 eV) is considered for the ionization via multiphoton process. The rate of multiphoton absorption is defined by the following equation [18]:

$$P(I)_{MPI} = \sigma_m \left(\frac{I}{\hbar\omega}\right)^m N_s, \tag{1.2}$$

where σ_m refers to m-photon absorption cross-section needed to excite an electron from the valence state to the conduction state, I is the laser intensity, $\hbar$ is the reduced Planck constant, ω is laser frequency and N_s is the atomic density of solids.

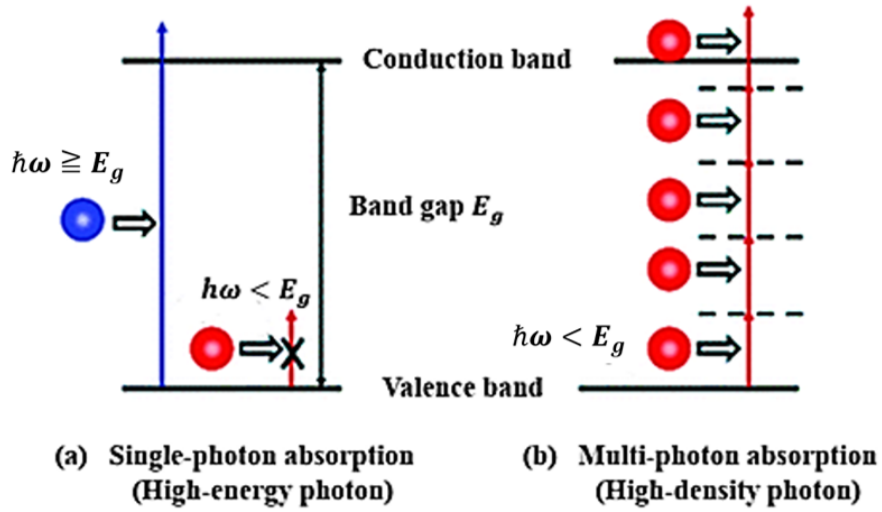

Figure 1.1: Single photon absorption where $\hbar\omega \geqq E_g$ and multiphoton absorption processes where $E_g > \hbar\omega$ [19].

At high laser intensities, a second process called tunnel ionization also comes into play. In tunneling ionization process, the energy bandgap decreases due to distortion in the band structure, leading to a direct electron tunnelling from the valance band to the conduction band as illustrated in figure 1.2.

Based on laser intensity and frequency, multiphoton excitation occurs in two different domains. Under strong laser field with low frequency, the tunneling ionization plays a dominant role in the interaction of femtosecond laser with matter, while at high frequencies, ionization is associated with multiphoton absorption. In terms of laser intensity, usually multiphoton absorption occurs at low laser intensities, however at high laser intensities, tunneling ionization plays a crucial rule in material ionization.

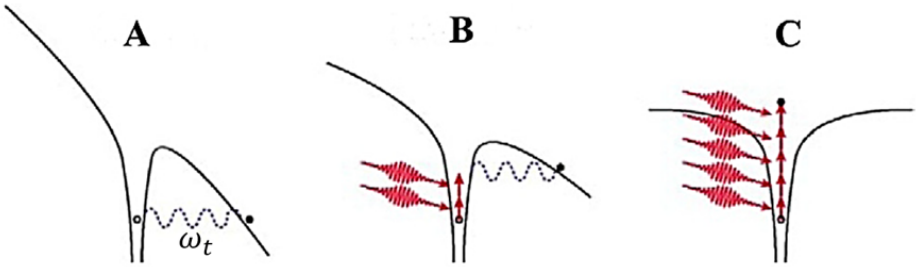

.

Figure 1.2: Schematic diagram of the photoionization of atoms induced by femtosecond laser pulse. A) tunneling ionization, B) mixing of multiphoton and tunneling ionization and C) the process of multiphoton absorption (MPI) [20]

Multiphoton absorption occurs at intensities of $\sim 10^{13}\ W/cm^2$. At even higher intensites of $10^{15}\ W/cm^2$, the electric field produced by the laser suppresses the Coulomb potential, resulting in free electrons by tunneling through the distorted valance band [21]. The multiphoton and tunneling ionization sometimes may happen at the same time as shown in figure 1.2.

The two mechanisms are governed by Keldysh's adiabatic parameter (γ) that specifies which of the two processes occurs [22]. Typically, the Keldysh parameter defines the ratio between the laser frequency (ω) to the frequency of a tunneled electron through a potential barrier (ω_t) and it is given by [23, 24]:

$$\gamma = \frac{\omega}{\omega_t} = \frac{\omega}{e}\sqrt{\frac{mcn\varepsilon_o\ E_g}{I}}, \tag{1.3}$$

where e is the electron charge, m is the electron mass, c is the light speed in vacuum, n is the material's refractive index, ε_o is the permittivity of the free space, E_g is the material's bandgap, and I is the intensity of the laser at the focus.

According to Keldysh parameter, if $\gamma > 1$, multiphoton ionization takes place,

while tunneling ionization most likely occurs when $\gamma < 1$. If the value of γ is close to 1, both processes occur simultaneously [24].

- **Avalanche ionization (AI)**

  In addition, another process known as avalanche ionization (AI) occurs when the excited electrons absorb multiple photons sequentially, resulting in high kinetic energy. Avalanche ionization is initialized via the seed electrons, which typically exist in the conduction band as a result of either thermal excitation or multiphoton or tunneling absorption processes. Through direct collision, excess energy is released by the seed electrons which further ionizes other electrons to higher energy excited states, generating two free electrons as schematically illustrated in figure 1.3, this process is referred as (collision) impact ionization. The above process is repeated by the two resultant electrons in the conduction band to ionize more electrons, leading to an increase in the number of free electrons in the conduction band exponentially, which is referred as avalanche ionization. This process results in a dense electron plasma that facilities the transfer of photon energy to the transparent materials.

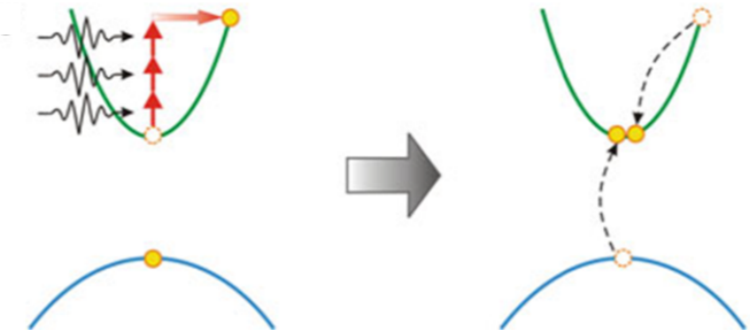

Figure 1.3: The process of avalanche ionization [25].

The free electron density behavior in the conduction band can be defined via the following rate formula:

$$\frac{dn(t)}{dt} = \alpha I(t)n(t) + \sigma_m I^m(t), \tag{1.4}$$

where $n(t)$ refers to electron density, $I(t)$ is the time-dependent laser intensity, α is the avalanche ionization coefficient, σ_m is the cross-section of m-photon absorption and m is the number of photons required to overcome the bandgap of the material. Avalanche ionization is assumed to be linearly proportional to the intensity of the electric field shown by the first term on the right side of equation (1.4) [23]. The longer the presence of the electric field, the more electrons will be elevated to the conduction band. The rate of AI is defined by the first term on the right side of equation (1.4) and the rate of MPI is strongly related to its intensity, as shown in the second term on the right side of equation (1.4).

After the nonlinear interactions, the electrons transfer part of their absorbed energy to the lattice through electron-phonon coupling within a timescale of picosecond. Then, a shockwave spreads in the surrounding lattice from the focal volume on a nanosecond timescale, followed by thermal diffusion in which the absorbed energy is distributed out of the illuminated area. Melting or non-thermal effect followed by solidification produce a permanent material modification.

1.3 Plasma formation and electron-lattice coupling

The generation of free-carrier via nonlinear process results in the formation of electron-ion plasma. The electrons (free-carriers) accumulate in the conduction band until the plasma frequency approaches the frequency of the incident light. The plasma density under this condition is defined as the critical plasma density ($N_{cr} = 10^{21} cm^{-3}$) [18]. Through free-carrier absorption, the dense plasma absorbs

the laser energy [23] while a small portion of the incident laser is reflected by the electron plasma. The frequency of the plasma (ω_p) is expressed by the following equation:

$$\omega_p = \sqrt{\frac{e^2 N_e}{\epsilon_o m^*}} \tag{1.5}$$

N_e is the electron density, e is the electron charge, m^* is the effective electron mass and ϵ_o is the electric permittivity.

When the pulse is gone, the electron-lattice relaxation process starts in which the electrons transfer their absorbed energy to the cold lattice thorough electron-phonon coupling phenomenon on a timescale of picosecond. When the material temperature reaches to a certain threshold temperature, the bonds are broken, leading to material ablation or permanent alteration of the structure in the bulk such as a change in the refractive index.

1.4 Material modification

A permanent material modification occurs within the material if the amount of deposited energy into the material is high enough to initiate the nonlinear processes. The material modification can be classified into a smooth modification of refractive index, formation of periodic nano-structures or generation of micro-explosion that leads to void formation [26].

The smooth alteration of the refractive index occurs at low laser intensities, slightly above the energy threshold of the material. Several mechanisms have been introduced to explain the smooth modification of the refractive index within dielectric transparent materials upon the femtosecond laser pulse irradiation. One mechanism that has been recorded in fused silica is related to the localized melting that

occurs on a nanosecond timescale, then followed by a fast re-solidification within the focal volume, i.e., inside the silica surface. Resulting density variation that leads to refractive index modification [27]. The birefringent refractive index change is generated as a result of the formation of self-organized periodic nano-structures (principle of such phenomenon is explained in details in chapter 4). Finally, when high pressure is generated in the middle of the laser-irradiated zone, a void formation occurs. If the pressure is greater than the young modulus of the solid material, a shock wave is produced which spreads in the lattice, leading to a void formation within the focal zone.

When the pulse energy density is high enough to overcome the material ablation threshold, laser ablation takes place on the surface in which the material is ejected from the target sample [28]. The laser ablation of dielectric materials can be explained in term of Coulomb explosion and thermal vaporization [28]. At low laser intensities close to the ablation threshold, the Coulomb explosion plays a significant role. When the electrons obtain enough kinetic energy, they eject out from the surface of the material. Consequently, an electrical field is generated because of the charge separation between the moving electrons and their ionized parent ions at the sample surface. The charge separation occurs when the absorbed energy via electrons overcomes the Fermi energy of the material. When the binding energy of ions in the lattice is lower than the electron energy, the ions are pulled out of the target via the local electric field, yielding in the removal of several nanometers depth of the lattice and thus a smooth surface is obtained [28].

Further, as electrons are generated in the conduction band, a strong phonon emission is induced. A few picoseconds after the end of laser pulse, the electron-lattice system reaches thermal equilibrium. At this time, the material within the focal zone undergoes explosion and various phenomena are initiated such as melting, decomposition and photomechanical ejection.

1.5 Femtosecond vs nanosecond laser pulse duration

Time Duration of pulse laser (τ) is one of the pivotal laser parameters that influences the material ablation process. In general, during the interaction of laser with matter, the laser energy is absorbed by the electrons, subsequently, the absorbed energy is transmitted to the material lattice through electron-phonon coupling. Cooling time (time taken to relax back to initial energy state) of electron which is in order of picosecond timescale is much longer than the heating time of lattice as thermal capacity of lattice is greater than the electron thermal capacity which is given by $C_e = (\pi^2 K_B^2 T_e)/(2E_f)$ in which k_B is the Boltzmann constant, T_e is the electron temperature and E_f is the Fermi energy.

In long pulse domain where the pulse width is greater than nanosecond, the width of laser pulse is much longer than the electron cooling and the lattice heating times. When nanosecond pulse laser is incident upon a material, laser energy is absorbed by the electron and energy absorbed is subsequently transferred to the lattice before the end of nanosecond pulse. Thus both the electrons and the lattice are approximately at the same temperature, hence, the thermal equilibrium can be expected. Usually with long pulsed laser, a significant amount of melting accompanied with vaporization and sometimes the occurrence of phase transition at high energy of laser pulse is observed. When the intensity of nanosecond laser is adequate to initiate material ablation, the velocity of ejected ablated particles is about μm/ns, leading in partial screening of the trailing edge of the pulse by the ablation plume which is the ejected ionized particle belonging to the material [29]. Therefore, less-controlled modified region is generated with ejected particles accumulation around the ablated area as a result of laser plasma plume ablation.

On the contrary, due to its short pulse width, the laser machining mechanism with femtosecond laser is quite different from the long pulse laser. With ultrafast pulse laser ($\tau \leq$ 10ps), the ablated area is drastically improved in contrast with nanosecond pulse. The smaller interaction volume is attained using ultrashort laser pulse which is attributed to the absence of thermal diffusion effect and the nonlinear absorption. The excitation processes in femtosecond regime occur in a timescale of $\sim$ 100 fs which is shorter than the electron-phonon relaxation time. Because the heat capacity of electrons is low, its temperature can be increased to greater than 10^3 K during the interaction of femtosecond laser pulses. Whenever the intensity of femtosecond laser reaches the lattice energy, i.e., energy required to separate ions from its bond, it results in modification of the target material. Since the breaking of bonds occurs instantly, there will not be enough time for energy dissipation to the lattices, resulting in a direct solid to gas phase transition and subsequently less heat-affected zone (HAZ) compared to the case with longer pulse duration. Although, the melting process can be noticed during the interaction of ultrashort pulses with very high pulse energies.

When the laser interacts with materials, initially the laser energy is absorbed in a layer within a dimension of optical skin depth which is given by $L_s = \frac{1}{\beta}$ in which β is the material absorption coefficient. The deposited energy is then transmitted out further deep in a lattice measured by the heat diffusion layer which is given by $L_d = \sqrt{DT_L}$, D is the heat diffusion constant and T_L is the laser pulse duration. The case at which $L_d > L_s$ is applied in case of long pulse laser, while with ultrafast pulses, diffusion does not spread to a depth larger than the skin depth $L_d < L_s$, leading to a direct solid-vapor transition [30].

Material micromachining with ultrashort laser provides high precision and cleaner morphology with minimal heat-affected-zone, in contrast to heat-affected-zone generated with longer laser pulses as shown in figure 1.4 (comparing between

two micro-structures generated in two different temporal regimes).

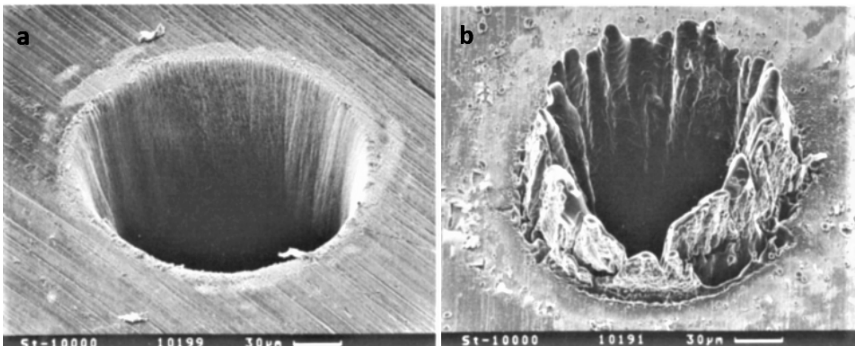

Figure 1.4: Laser ablation of a 100 μm thick steel foil with a) 200 fs, 120 μJ pulses energy at 780 nm and b) 3.3 ns, 1 mJ pulse laser at 780 nm [31].

1.6 Incubation effect

The formation of precise micro-structures on or inside a wide range of materials can be realized using femtosecond laser material processing. In multiple pulse regime, several studies reported that irradiating materials surface with a train of ultrafast pulses lowers the ablation threshold which is the minimum laser fluence needed to initiate the ablation process. This effect was first reported during the interaction of multiple nanosecond laser pulses with metals [32]. The most likely accepted scenario underlying the physical mechanisms of incubation is after the irradiation of multiple laser pulses, the surface roughness increases due to the formation of ripples, accumulation of surface defects and the heat accumulation in the material. The repetitive defects generated because of changes in the material's chemical, mechanical and optical characteristics, within the irradiated region. Thus, micromachining with high repetition rate lasers allows heat accumulation from shot to shot and therefore enhancing the ablation and material removal at low pulse energies. In such a process, the modification or removal of the material occurs at lower threshold energy. When the first pulse that hit the surface generates such defects, they facilitate the absorption of subsequent pulses, therefore enhancing the material ablation rate. As the

number of laser pulses increases, the threshold fluence decreases due to the effect of heat accumulation. The ablation threshold fluence of multiple pulses of a material (F_{th}^{N}) is related to the ablation threshold of a single pulse (F_{th}^{1}) as follows [33]:

$$F_{th}^{N} = F_{th}^{1}\ N^{S-1}, \tag{1.6}$$

where S is the material incubation effect.

The incubation model [34] states that a significant number of pulses causes the threshold fluence of multiple pulses to approach zero. The occurrence of saturated incubation effect and the constant threshold fluence were reported when the number of pulses was greater than 1000 pulses, meaning no further decrease in threshold fluence. This result does not agree with equation (1.6), thus a modified incubation model was introduced to describe the saturation of threshold fluence with an infinite pulse number which is given by:

$$F_{th}^{N} = F_{th}^{\infty} + \Delta F_{th}^{1,\infty} N^{S-1}, \tag{1.7}$$

where $\Delta F_{th}^{1,\infty}$ is the difference between the threshold of a single pulse and the threshold with an infinite number of pulses, F_{th}^{∞}.

1.7 Laser parameter

Material modification during femtosecond laser interaction is primarily due to nonlinear absorption. Since nonlinear absorption phenomena is highly dependent on the laser intensity threshold, intensities higher than the breakdown threshold is required. In order to satisfy this condition, high numerical aperture (NA) objective lens is used to focus the femtosecond laser pulse with intensities up to $10^{13}\ W/cm^2$ within the focal volume. Assuming a Gaussian profile laser beam is focused onto a

material via objective lens, the waist radius of the beam (w_0), at its smallest point which is half the diameter of the spot size, is given by:

$$w_0 = \frac{M^2 \lambda}{\pi N A}, \tag{1.8}$$

where M^2 is the beam quality factor which can be 1 for pure Gaussian and λ is the light wavelength.

The Rayleigh length which is the distance from the waist of the beam to the point where its width is doubled is given by:

$$z_R = \frac{\pi \ w_0^2}{\lambda}. \tag{1.9}$$

Therefor, the peak laser intensity I_{peak} (i.e., the intensity on the laser beam axis) can be expressed as:

$$I_{peak} = \frac{P_{peak}}{\pi w_0^2}, \tag{1.10}$$

where the peak power P_{peak} is given by:

$$P_{peak} = \frac{E}{\tau}, \tag{1.11}$$

where E and τ are the pulse energy and the pulse duration, respectively.

1.8 Previous works

Laser ablation by ultrashort laser pulses has been previously used to structure the surface of diamond to fabricate laser-induced periodic surface structures (LIPSS) and periodic arrays of spiral. LIPSS are periodic structures that have a spatial period significantly smaller than the laser irradiation wavelength. They were generated on different materials such as metal, semiconductor and transparent dielectric mate-

rials by irradiating the material with multiple number of ultrafast laser pulses near the material threshold. With the increasing number of industries that grow synthetic diamond by either CHEMICAL VAPOUR DEPOSITION (CVD) or HIGH-PRESSURE HIGH-TEMPERATURE diamond (HTHP), researchers have been exploring diamond properties for the future applications. It has been proven that micromachining on diamond surface with high precision, minimal surface roughness is considerably a very complex process. Therefore, laser machining of diamond has become crucial, especially in implementation such as microelectronics and cutting tool industries.

A study by Shinoda et al. [35] explored the formation of sub-wavelength surface structures on CVD single crystal diamond using femtosecond laser pulse at central wavelength of 800 nm operating at 250 kHz and 120 fs. For single crystal diamond with pulsed laser at 800 nm, the laser intensity must be of the order of $2 \times 10^{16}\ W/m^2$, as to start the ablation processes. Because of the large bandgap of diamond, a dense plasma was generated via nonlinear ionization processes, followed by the interference between the incident light and the laser-induced plasma that led to the fabrication of linear periodic surface structures shown in figure 1.5 which were perpendicular to the laser polarization and with periodicity of $\frac{\lambda}{2n} \sim (146 \pm 7)nm$ where n is the material refractive index. They observed a maximum length of periodic linear grooves of millimeter length. By scanning the laser beam over the target, the grooves can be extended to a length of 0.3 mm.

Above the ablation threshold, structures with micrometer width were formed, while below the ablation threshold, grooves of nanometer width were observed. Cleanest morphology and identical grooves were obtained approximately at the ablation threshold. The ratio of the width to the depth of grooves which was 40 nm to 500 nm is larger than 12, which can be varied by changing the laser repetition rate and the speed of laser scanning. Also, the ablated region was characterized by Ra-

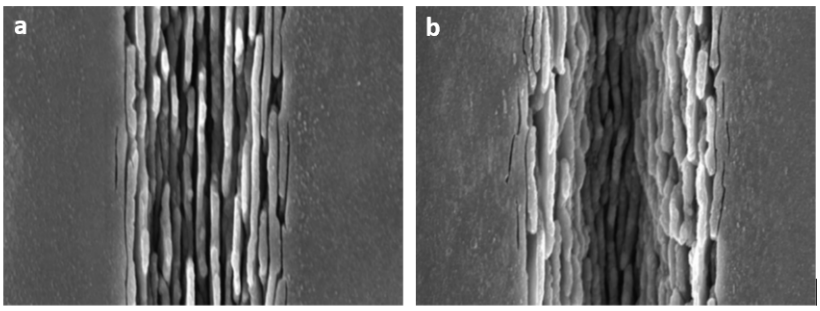

Figure 1.5: Scanning electron microscope (SEM) images of the diamond surface after the irradiation of a 1000 pulse train of 120-fs laser pulses at a repetition rate of 250 kHz with a pulse energy of a) 80 nJ and b) 120 nJ [35].

man spectroscopy to prove no structural changes in the original diamond structures within the focal volume occurred after treating the material with femtosecond laser. Unlike the case with longer pulses, the Raman spectrum of the irradiated region with femtosecond laser presents the original diamond peak at 1331 cm^{-1}, meaning the material after irradiation maintained the original diamond composition as shown in figure 1.6. Because diamond has a large bandgap, it usually experiences a phase transition to become opaque to the incident light during the laser ablation process with longer pulse duration. A phase transition from diamond to graphite is observed with long pulse duration, while with ultrashort laser pulse the material at the irradiated region preserved the original diamond structure [36].

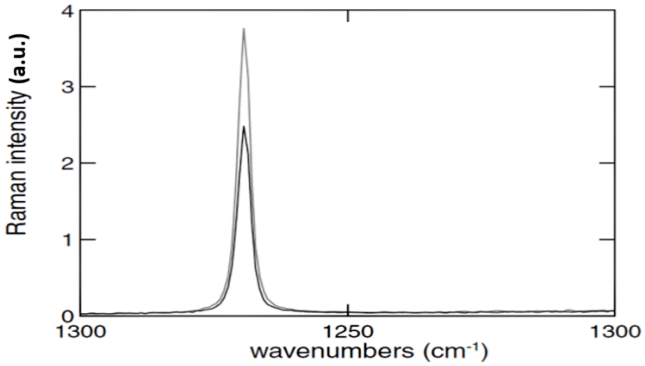

Figure 1.6: The Raman Spectra of the irradiated diamond sample (black) and unirradiated region (gray) [35].

In another study [37], researchers illustrated the formation of nano-spirals on diamond surface using high repetition femtosecond laser pulse of 50 MHz at 1040 nm. With higher repetition rates, a great number of laser pulses are delivered to the target surface, leading to a deep concentrated ablated area in the form of hole due to the extreme heat accumulation effect without any nano-ripples at the boundary of the ablated area in contrast to the case with low repetition rate laser pulse. Therefore, taking into consideration the correct laser parameters such as laser polarization and material properties, they were able to fabricate nano-ripples at the inner wall of the ablated region on a natural diamond. Using circular polarization state of light with varying pulse energies, nano-spiral structures that appear as a periodic strip array at the inner wall of the irradiated area with a periodicity of sub-micrometer scale were formed as shown in figure 1.7.

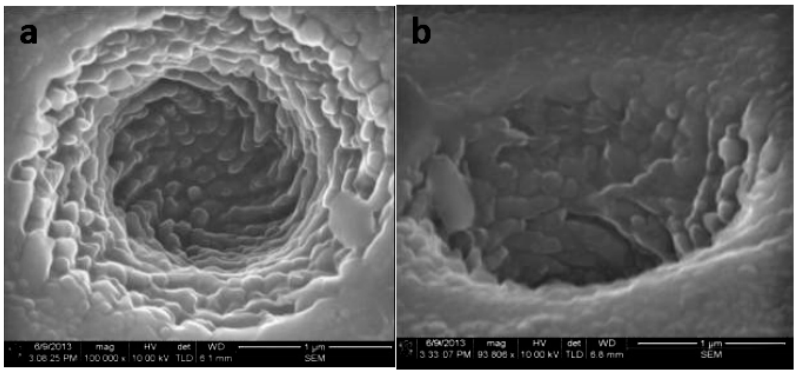

Figure 1.7: SEM images of the ablated region generated by circular polarization fs laser pulses a) the surface at 0° and b) rotated by 52° [37].

Chapter 2

Orbital angular momentum beam

Understanding that a beam of light can have orbital angular momentum (OAM) in addition to spin angular momentum (SAM) has led, in the last decade, to novel experiments in quantum mechanics and new techniques for probing, manipulating [38], imaging microparticles [39], etc. Such characteristic allowed the beams to be more tightly focused than ever recorded. For example, a light with radial polarization distribution improves the focus more than the conventional linear polarized light does [40].

The distinguishing feature of such light beams is their helical phase front. The twisted modes of the electrical field are characterized by a helical-shaped wavefront with a null-intensity, i.e., optical vortex or a topological defect, at the beam axis. While the SAM is associated with the polarization state of light and has a magnitude of $\pm\hbar$ per photon in which the sign refers to the right and left circular polarization, the OAM of light can be attributed to the helical phase front of such beams as component of Poynting vector, which describes the magnitude and direction of the energy flow and is always vertical to the wavefront. Such light beams with an azimuthal phase dependence, exp $(i\ell\phi)$, have OAM independent of the polarization

state of beam where the angle ϕ is the azimuthal coordinate along the cross-section of the beam. Such beams possess OAM value of $\pm\ell\hbar$ per photon, where the sign indicates the beam handedness with respect to the beam's axis and ℓ is an integer number that indicates the number of the distinct but intertwined helix with a length equal to the wavelength of the beam for each helical surface. When $\ell = 0$, the wavefront is not twisted and consists of a series of parallel planes, i.e., Gaussian beam. For $\ell = \pm 1$, the wavefront is formed as a single helical surface within a wavelength and so on as indicated in 2.1.

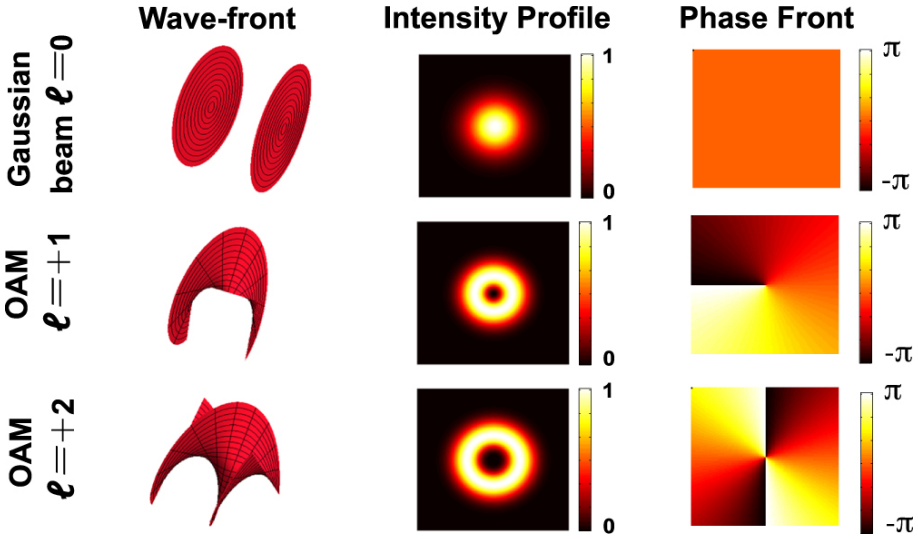

Figure 2.1: shows wave-front, intensity profiles, and phase front for different order of Gaussian beams [41].

2.1 Laguerre-Gaussian mode

The polarization distribution of light is the vectorial dependent property of the electric field. The cross-section of a beam can have a spatially homogenous polarization or inhomogeneous polarization. Polarizations like linear, circular or elliptical polarization are the examples of homogenous polarization, whereas inhomogeneous polarizations include radial or azimuthal like polarizations. An example of a beam with spatially varying polarization having cylindrical symmetry is the vector Laguerre-Gaussian (LG) beam. A LG beam is uniquely characterized with its helical-shaped

wavefront and an optical vortex in the center, at the beam axis that is associated with the topological charge (as presented in this work). Laguerre-Gaussian modes in cylindrical coordinates (r,ϕ,z) are given by:

$$\mathbf{U}(r,\phi,z) = \frac{C_{\ell p}^{LG}}{w(z)}\left(\frac{r\sqrt{2}}{w(z)}\right)^{|\ell|} exp\left(\frac{-r^2}{w^2(z)}\right) L_p^{|\ell|}\left(\frac{2r^2}{w^2(z)}\right)\times \\ exp\left(\frac{-ikr^2}{2R(z)} - i\ell\phi - ikz + i\psi(z)\right), \tag{2.1}$$

where ℓ and $p \geq 0$ are the azimuthal index and the radial index, respectively. $\mathrm{L}_{\mathrm{p}}^{\ell}$ is the associated Laguerre polynomials, $C_{\ell p}^{LG}$ is a normalization constant, $R(z)$ is the radius of the wavefront curvature, $w(\mathrm{z})$ is the beam radius along the propagation direction z, k is the wave number and $\psi(z)$ is the Gouy phase.

2.2 Orbital angular momentum beam generation

Production of light with helical wavefront requires an optical element that adds a phase shift to the cross-section of the incident beam [42]. Several methods exist for the generation of vortex beams carrying OAM. Mode conversion is the first technique, proposed by Allen et al. to imbue an optical beam with OAM. In this method, inside the laser cavity, the Hermit-Gaussian beam is converted into a pure Laguerre-Gaussian beam via propagation through cylindrical lenses [43]. This technique requires the output of the laser to be a higher-order mode of Hermite-Gaussian to produce the desired order of LG beam.

From then, several methods have been proposed to optimize the generation of OAM beams, including spiral phase plate (SPP), diffraction grating, and q-plate. The SPP is an optical device that has a gradually increasing gradient surface as

shown in 2.2. It is made up of a dielectric material whose thickness increases spirally around the center of the plate creating a phase gradient on the beam during propagation. The thickness of the SPP increases proportionally with respect to the azimuthal angle (ϕ) of the plate. By varying the height of the step (h), the phase shift imprinted on the wavefront of a plane wave is controlled, resulting in a phase shift of an integer (ℓ) multiple of 2π. Therefore, the azimuthal mode number (topological charge ℓ) is related to the step height of the SPP as follows:

$$\ell = \frac{h\ (n_1 - n_2)}{\lambda}, \tag{2.2}$$

where n_1 and n_2 are the refractive indices of the plate (SPP), and the surrounding medium (air), respectively. h is the height between the thinnest and the thickest surface in the spiral surface. Despite the simplicity of the SPP, fabricating such a surface is not economical and requires a high machining precision at the optical wavelength [44].

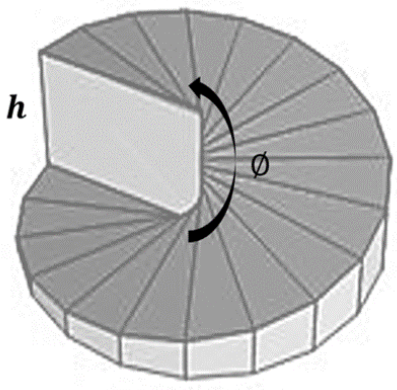

Figure 2.2: Spiral phase plate (SPP).

Second mothed is the fork diffraction gratings, especially after the emergence of meta-surfaces that provide planar and simple solutions. The diffraction grating consists of numerous bars in which the number of lines at the top is different from the lowest part, leading to a fork-dislocation as depicted in figure 2.3. If the difference between the top and bottom is one line that looks like ''Y", the plane wave will acquire an OAM value of $\ell = 1$. The higher the difference between the number of lines at the top as compared to the below part of the diffraction grating, the higher the OAM is generated. Figure

2.3 shows the output of first, second and third order OAM beams generated with a Gaussian beam (0th-order of OAM) as input. Similarly, like SPP method, each diffraction grating is designed to generate a specific order of vortex beam. However, the diffraction grating technique is not restricted to a given wavelength.

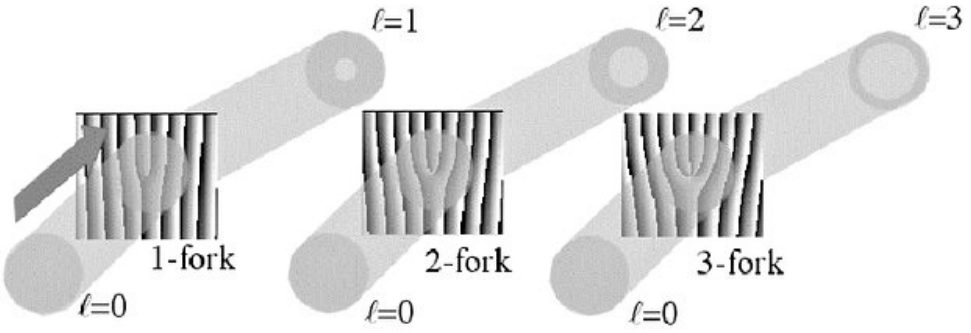

Figure 2.3: Forked diffraction grating with 1, 2 and 3 fold-dislocations at the center and the generated OAM beams with their corresponding OAM values [45].

In 2006, Marrucci et al. introduced a novel device that can produce an optical beam with well-defined OAM depending upon the polarization state of the input light called as q-plate [42]. In this thesis, OAM beams are generated by q-plate which will be discussed in more details in the upcoming section.

2.2.1 The concept and technology of the q-plate

Q-plate has been widely used to produce OAM eigenstates related to the beam with helical wavefront in applications such as metrology, advance experiments in quantum mechanics and microscopy, etc. The advantages of using q-plate over other techniques is the flexibility to obtain the desired state of polarization in the output state by changing the polarization state of the incident beam, the ability of coupling spin to orbital angular momentum and efficiency in terms of converting SAM to OAM through its robust tuning mechanism by simply using an external voltage.

The q-plate is an electro-optical device with birefringent retardation (δ) con-

trolled by an external voltage. It is made up of LC (liquid crystal) film enclosed between two glasses which is a transparent conducting material, allowing the flow of current from the voltage supplier to the q-plate for electrical tuning.

The principle of q-plate is characterized with a topological charge (q) which is named after it, a uniform birefringent retardation phase (δ) and an optic axis that has a singular pattern with a specific topological charge (q) in the transverse plane and a defined initial orientation (α_0). The optical axis of the q-plate in the polar coordinate (r,φ) can be expressed by [46]:

$$\alpha(r, \varphi) = q\varphi + \alpha_o, \tag{2.3}$$

where α is the formed angle between the optics axis and the x-axis at each spot in the plate and φ is the azimuthal angle, and α_o specifies the initial molecular orientation of the liquid crystals (molecular director) with respect to a reference axis.

Working of the q-plate can be explained as separation of the incident polarized light into two components, perpendicular to each other, then delaying the phase of one of the components relatively to the other. Recombination of the two components takes place to form a vortex beam carrying unique OAM in a unit of $\hbar$. When a light beam propagates through the liquid crystal q-plate, it will twist and acquires an OAM value of $2q\hbar$ per photon. The handedness of the output beam is determined by the input light polarization. Further, the SAM to OAM coupling efficiency of q-plate is governed by its optical retardation factor (δ). Q-plate action on the input Gaussian beams can be determined by the following formula: (input polarization is considered in the circular polarization basis) [47].

$$E_{out} = \ cos\ (\frac{\delta}{2})\begin{pmatrix} e_L \\ e_R \end{pmatrix}\ + i\ sin\ (\frac{\delta}{2})\begin{pmatrix} e_R\ e^{+\ 2i(q\varphi\ +\ \alpha_0)} \\ e_L\ e^{-2i(q\varphi\ +\ \alpha_0)} \end{pmatrix}. \tag{2.4}$$

If $\delta = \pi$, the result as expressed in the equation (2.4) is full conversion of the incident beam into OAM beam which is called the tuned state of the q-plate and partial conversion takes place when $\delta \neq \pi$ (partially detuned state of the q-plate). The handedness is flipped after passing the q-plate as shown in figure 2.4 with two different q-plates.

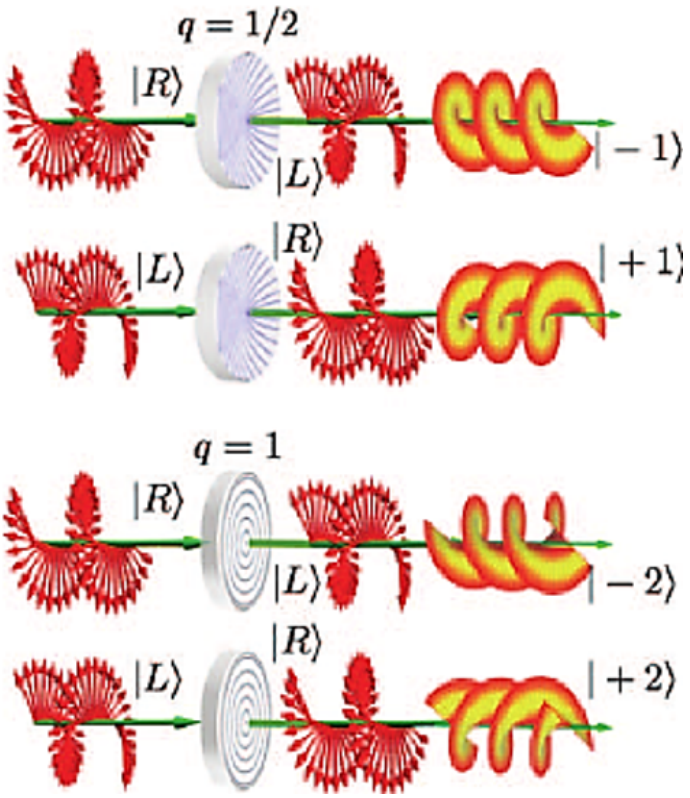

Figure 2.4: The effect of different orders of q-plate on circularly Gaussian beams [46].

In case of a linearly polarized beam, the action of the q-plate can be explained as follows: when a linearly polarized beam, as the input beam, passing through a q-plate with 0.5 topological charge, the output beam is radial or azimuthally polarized beam. These beams can be considered as a combination of two helical waves having the same magnitude of OAM with $\ell = 1$ (in this case) but of opposite polarity.

2.3 The polarization state of light

Polarization of light plays a pivotal role in almost all of the photonics implementations. For example, optical microscopy, spectroscopy, optical communication and optical trapping, etc. The polarization state of light is defined as the orientation of the electric field vector which is always perpendicular to the propagation direction of light. When the director of the electric field vector describes an ellipse in any fixed plane intersecting and normal to the direction of propagation of light such a polarization state is called an elliptical polarization. Various other types of polarization, such as linear and circular, can be described as the special case of elliptical polarization. The axis of the ellipse is distinguished by the semi-major (a) and semi-minor (b) axes as shown in the left schematic diagram in figure 2.5.

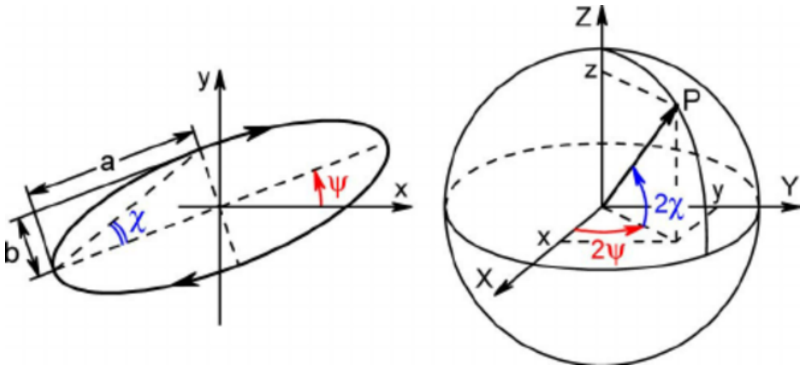

Figure 2.5: Polarization ellipse and the Poincaré Sphere [48].

The angles represented in the elliptical system are the azimuthal angle (Ψ) and the ellipticity of the polarization ellipse (χ). The azimuthal angle indicates the rotation of the ellipse from the x-axis to the semi-major axis of the ellipse. The ellipticity (χ) of the polarization ellipse that measures the degree of deviation from the shape of a circle and in ellipse coordinate system is given by the length of the semi-minor axis divided by the semi-major axis of the ellipse as shown in equation (2.5):

$$\chi = \pm\frac{b}{a}, \tag{2.5}$$

where ellipticity is positive when the rotation of the electric field vector is clockwise and negative for the anti-clockwise rotation.

Although these two parameters seem to be the straightforward mothed to decribe various polarization states of light, in fact, the two parameters are not directly measurable. What can be measured is the four Stokes parameters. The Stokes parameters can be measured directly by analyzing the light intensity subjected to various optical devices like waveplates and polarizers and they are defined by the following equations [49]:

$$S_0 = E_{0x}^2 + E_{0y}^2, \tag{2.6}$$

$$S_1 = E_{0x}^2 - E_{0y}^2, \tag{2.7}$$

$$S_2 = 2E_{0x}E_{0y}\ cos\delta, \tag{2.8}$$

$$S_3 = 2E_{0x}E_{0y}\ sin\delta, \tag{2.9}$$

where S_0 parameter is the quantity that represents the total light intensity (I) and δ is the relative phase between the orthogonal component of the electric field and when $S_0 = \sqrt{S_1^2 + S_2^2 + S_3^2}$ means fully polarized light and when $S_0 > \sqrt{S_1^2 + S_2^2 + S_3^2}$ means the light is partially polarized or unpolarized.
S_1 describes the linear horizonal polarization (LHP) and the linear vertical polarization (LVP).
S_2 describes the diagonal polarization (D) and the anti-diagonal polarization (A).
S_3 describes the right circular polarization (RCP) and the left circular polarization (LCP).

From the stokes parameters, we can derive the polarization ellipse in terms of the orthogonal components of the electric field, according to the relation:

$$tan\ 2\Psi\ =\ \frac{2E_{0x}E_{0y}}{E_{0x}^2 - E_{0y}^2}\ cos\delta\ =\ \frac{S_2}{S_1}, \tag{2.10}$$

where Ψ takes values between $\left[\frac{-\pi}{2}, \frac{\pi}{2}\right]$ and $\delta = \delta_y - \delta_x$ is the phase difference between the two orthogonal components. In addition, the ellipticity can be expressed as:

$$sin\ 2\chi = \frac{2E_{0x}E_{0y}}{E_{0x}^2 + E_{0y}^2}\ sin\ \delta = \frac{S_3}{S_0}. \tag{2.11}$$

Assume that we have linear horizontally polarized (LHP) light then according to the definition of each Stokes parameter, the Stokes parameters for the LHP in the absence of the vertical component are as follows:

$$S_0 = \ E_{0x}^2\ ,\ S_1 = E_{0x}^2\ \ and\ S_2 = S_3 = 0. \tag{2.12}$$

Further, the most significant development in the polarization theory was when Henri Poincaré invented a more convenient graphical tool to describe the light polarization in term of polarization ellipse and Stokes parameters. The three Stokes parameters (except S_0), can be mapped in a 3D unity spherical sphere as shown in figure 2.5. The conversion from Cartesian to spherical coordinate according to equations 2.13, 2.14 and 2.15 is required to present the polarization ellipse into the sphere which also explains the factor of 2Ψ (latitude) and 2χ (longitude).

$$x = cos\,(2\chi)\,cos\,(2\Psi)\,. \tag{2.13}$$

$$y = cos\,(2\chi)\,sin\,(2\Psi)\,. \tag{2.14}$$

$$z = sin\,(2\chi)\,. \tag{2.15}$$

The polarization distribution of light can be represented by a point on the surface of the so-called Poincaré sphere and the degree of the polarization is determined by the distance from the surface to the origin. For example, unpolarized beam lo-

cated at the origin of Cartesian coordinator of the sphere, as moving toward the surface, the light is partially polarized until it gets on the surface which corresponds to a fully polarized beam. While the two independent factors (ϑ,φ) defined in figure 2.6 in spherical coordinator, where φ, ϑ are the azimuthal and polar angles, define the polarization state [50].

For a beam with uniform polarization states, the fundamental Poincaré sphere represented in figure 2.6 is used to describe the polarization patterns. North and south poles on the sphere denote the left (L) and (R) right circular polarization, respectively. Points on the equator correspond to all cases of linear polarization; e.g. horizontal (H), vertical (V), diagonal (D) and anti-diagonal (A). Any other points define the state of elliptical polarization.

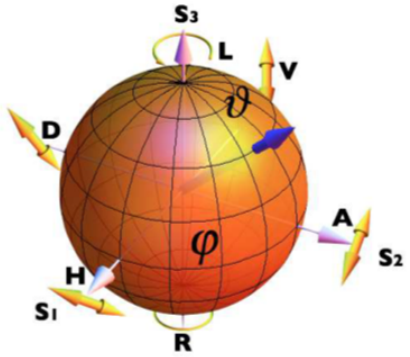

Figure 2.6: The fundamental Poincaré sphere with the corresponding H, V, D and A linear polarization at the equator and L and R circular polarization at the poles [51].

Most recently, a lot of scientific studies are carried out with the light having complex polarization states that vary spatially such as radial, azimuthal and spiral polarizations. To visualize such polarization pattern, higher-order Poincaré spheres were introduced in contrast to the uniform polarization state of light which can be represented on the fundamental Poincaré sphere. On the surface of first-order Poincaré sphere, north pole is circular polarization left with OAM of $\ell = -1$, and

south pole is circular polarization right with OAM of $\ell = +1$ while radial, azimuthal are denoted by the diagonally opposite points on the equatorial plane and spiral states by the points between equator and the poles on the surface of the sphere as shown in figure 2.7a. The same case for the second-order vortex beams (with OAM of $\ell = 2$) on the second-order Poincaré sphere shown in figure 2.7b [51]. Such spatially complex polarization state analysis requires measuring all the Stokes parameters. In this thesis, we are presenting a simple method to directly visualize the polarization state by mapping them onto a solid surface.

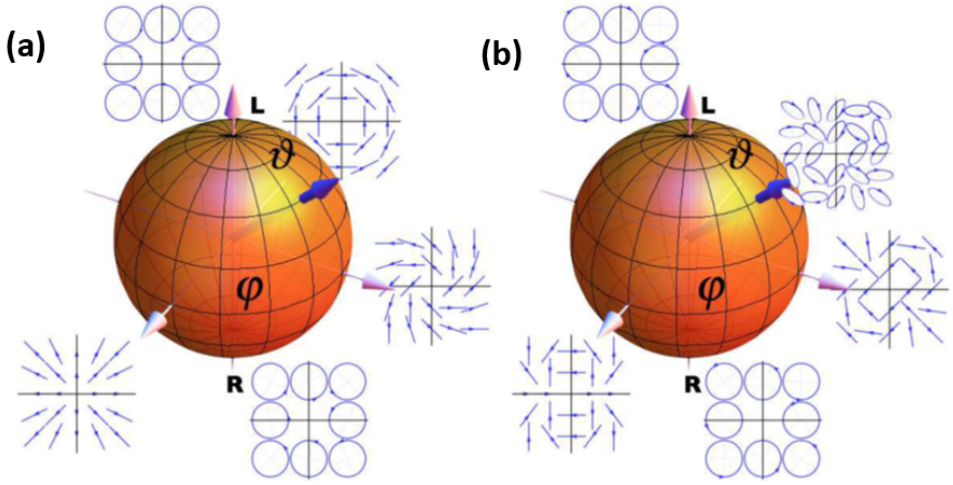

Figure 2.7: a) is the first-order Poincaré sphere with the corresponding first-order vortex polarization including radial, azimuthal and spiral at the equator and R, L circular polarizations at the poles and b) is the representation of second-order vortex polarizations which includes type-I and type-II at the equator and R and L circular polarizations at the poles [51].

Chapter 3

Experimental methods and setup

This chapter presents the details of the laser system, experimental setups and calibration methods used for the measurements. The section on the experimental setups contains details of experiments involving Gaussian and non-Gaussian laser beams.

3.1 Laser system

The laser used in our experiments is a Ti:Sapphire laser system consisting of a Ti:Sapphire oscillator and a regenerative amplifier. The oscillator is pumped by a 5W Nd:YVO_4 diode pumped solid state laser (Millenia, Spectra-Physics, 532 nm) and the amplifier is pumped by a 30W frequency-doubled Nd:YLF (Empower, Spectraphysics, 527 nm) laser. The laser oscillator produces pulses of 20 fs at 800 nm and 76 MHz repetition rate with an energy of $\sim$ 5 nJ. To avoid damage to the optics during the amplification processes, Chirped Pulse Amplification (CPA) technique is used to first stretch the femtosecond pulse to nanosecond, amplify and then recompress the pulse to femtosecond duration [52].

Chirped Pulse Amplification (CPA) allows a Ti:Sapphire crystal to be used

to amplify pulses beyond its damage threshold (peak power) by keeping the power density inside the amplifier below the damage threshold. CPA technique is a three-step process.

The first step- stretches the very short pulse seed coming from a stable, mode-locked femtosecond laser. Stretching the duration of the seed pulse by a large amount reduces its peak power, which reduces the chances of damage to the Ti:Sapphire crystal. This is because $Intensity = \frac{Energy\ (J)}{time\ (fs)\ \times\ area\ (\mathrm{cm}^2)}$. Therefore, reducing the duration by 10^6 reduces the intensity by 10^6.

The second step- amplification of the stretched pulse: a pump laser provides a coherent (synchronous) energy pulses to the Ti:Sapphire crystal, therefore, exciting it to higher energy state just before the arrival of the stretched pulse. The stretched pulse causes stimulated emission, further amplifying the pulse at the same wavelength.

The third step– the restoration of the amplified pulse as close as possible to its original duration by recompressing the stretched, amplified pulse.

The first step of stretching the laser pulse in time is accomplished by using a pair of gratings that are arranged in a way such that the low-frequency component of the seed pulse travels shorter path than the high-frequency component. The seed pulse becomes positively chirped after going through the grating pair, i.e., the higher-frequency component lags behind the lower-frequency component and has a longer pulse duration than the original one. Then the stretched pulse, whose intensity is considerably low in comparison with the damage threshold, is safely introduced to the active medium and amplified by a factor of a million or higher. Finally, the amplified laser pulse is recompressed back close to the original pulse width through a reversal of the process of stretching using a grating pair. Operational parameters of the laser system are shown in the table below:

Table 3.1: Laser system specifications

	Oscillator	Amplifier
Repetition rate	76 MHz	1 kHz
Pulse duration	20 fs	45 fs
Pulse energy	5 nJ	2.5 mJ
wavelength	800 nm	800 nm

3.2 Calibration of laser parameters

3.2.1 Pulse duration measurement

One of the factors affecting the laser ablation process is the duration of the laser pulse. In order to measure and calibrate the laser pulse duration, we reflect a small portion of the beam after it leaves the amplifier into an autocorrelator system that measures its pulse width. The autocorrelator system operates by splitting the pulse into two pulses using the beam splitter, then the two pulses overlap in a nonlinear crystal (BBO crystal), the path difference and thus the relative timing of the pulses can be manually adjusted via the delay line. If the path difference is made small, which results in the process of sum frequency generation, leading to an output beam with a higher frequency, i.e., the process of second harmonic generation (SHG) occurs. The second harmonic signal is detected by a camera that displays its spatial intensity. After converting the spatial intensity of the SHG signal into the autocorrelation signal, a numerical value of the pulse duration will be displayed on the computer. In the experiment, a series of dispersive optical elements are placed in the beam path as shown in the setup figure 3.6. When the ultrashort beam passes through a dispersive medium, it experiences a chirp that broadens its pulse duration which is due to the wide spectrum of the femtosecond pulses and the medium's group velocity dispersion (GVD) [53]. The GVD is a parameter that describes the effect of a dispersive medium on the duration of an optical beam passing through it.

A series of optical elements include beam splitter, half-wave plate (HWP),

polarizer, neutral-density filters (ND), and a glass slide. The splitter and the HWP are made of silica quartz that has a GVD of 36.16 fs^2/mm. The rest are made of BK7 which has a GVD of 44.65 fs^2/mm at a wavelength of 800 nm. By knowing the thickness of each element and their corresponding GVD values, we calculated the group delay dispersion GDD (as GVD is GDD per unit distance) usually written in a unit of (fs^2/mm). In addition, another HWP was placed to alter the polarization state of the beam and by substituting all the values in equation (3.1), we found that the pulse duration of the beam at the back of the objective lens aperture is 81 fs.

$$\tau = \tau_o \sqrt{1 + \left(\frac{GDD}{\tau_o^2} \, 4 \ln 2 \right)^2}, \tag{3.1}$$

where τ is the pulse duration after propagating through dispersive medium and τ_o is the original pulse duration.

To ensure the pulse duration at the sample is minimum, we introduced a negative chirp to the pulse. The duration at the sample was optimized by looking at the plasma when it is brighter.

3.2.2 Energy calibration

The energy per pulse delivered to the sample surface was controlled by a combination of HWP and a polarizing beam splitter. In addition, multiple neutral density filters were placed in the setup to further minimize the pulse energy. For controlling the pulse energy, the HWP was placed in a rotational stage connected to a computer, thus allowing the rotation of the plate in fine increments. Since the fast axis of the half-wave plate (in a rotational stage) was initially aligned parallel to the transmission axis of the cube polarizer, rotating the half-wave plate resulted in changing the beam power. In continues mode, the laser power was recorded prior to each experiment at different angles of the HWP. We finally obtained the pulse

energy on the sample surface by considering the transmission and reflection of the entire optical elements used in the setup and by applying the higher order polynomial curve fitting which can provides better accuracy in terms of approximation of the behavior of several natural occurring mathematical functions on the energy vs. angles curve in figure 3.1. Further, energy per pulse was obtained by dividing the calibrated power with the repetition rate of the laser beam.

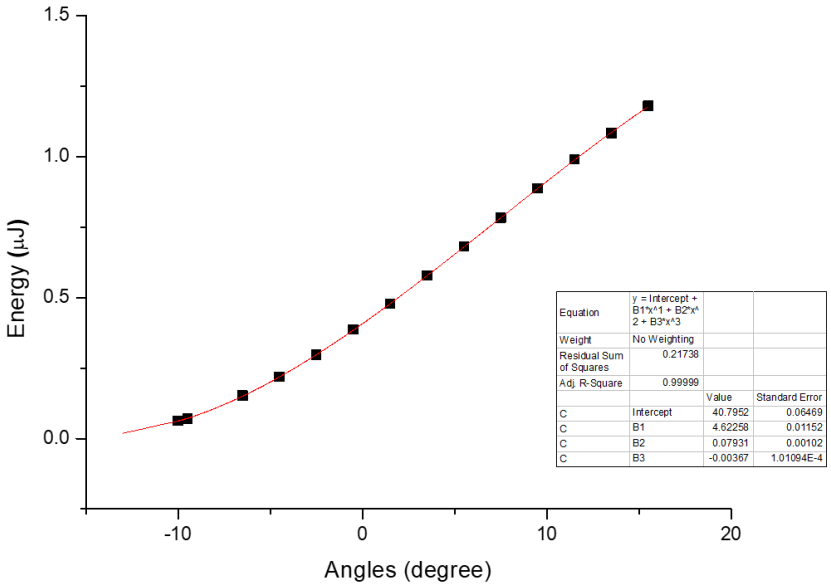

Figure 3.1: An example of energy curve calibration.

3.3 Fluences and focused spot size

In micromachining, many factors related to the input laser beam have a significant impact on the modified region, including the pulse duration, input beam polarization, the beam wavelength, the fluence and the focused spot size. Thus, an optimal characterization of the laser beam is important to understand its interaction with solids and thereby to enhance the efficiency of laser processing of materials.

During the interaction of a beam having Gaussian spatial intensity profile with matter, the laser energy deposited in a unit area of the material, i.e. fluence,

is expressed by the following equation [54]:

$$F_G(r) \;=\; \frac{2E}{\pi\ w_0^2}\ exp\ \left(\frac{-2r^2}{w_0^2}\right). \tag{3.2}$$

Since the peak intensity of the Gaussian beam is located at $r = 0$ (center of the beam), the peak fluence can be written as:

$$F_{G,Peak}(r=0) \;=\; \frac{2E}{\pi\ w_0^2}, \tag{3.3}$$

where E is the pulse energy and w_0 is the beam waist. Experimentally, in order to estimate the fluence (J/cm^2) and the fluence threshold (the minimum energy at which we notice a change in the laser-affected zone) [18], we performed a single shot experiment on the HPHT single crystal diamond surface with varying pulse energies. The fluence threshold was determined by directly measuring the diameter of the ablated area and taking its ratio with the pulse energy.

A Gaussian beam can be confined to a minimum focused spot size due to its low divergence. An objective lens with a given numerical aperture (NA) in the air allows the beam with a wavelength of λ to focus to a diameter D given by [55]:

$$D = \frac{1.22\ \lambda}{NA}. \tag{3.4}$$

The beam waist or focused spot size is expressed as the radius of the beam measured from the center of the beam to the point where the intensity of the beam drops by $1/e^2$ of the maximum intensity.

The focal spot size of a Gaussian beam was estimated experimentally by plotting the square of the beam diameter (D^2) as a function of pulse energy (E) with respect to the ablation threshold of the material (E_{th}), which is the minimum en-

ergy that causes a visible material modification. A linear fit is performed to the experimental data points shown in figure 3.2 according to the equation:

$$D^2 = \frac{D_0^2}{2} ln\left(\frac{E}{E_{th}}\right). \tag{3.5}$$

We obtained the slope which corresponds to $\frac{D_0^2}{2}$ in which the radius of the beam is $w_0 = \frac{D_0}{2}$. The radius of the focal spot size was measured to be (2.25 ± 0.8) μm compared to the theoretical value of 1.95 μm calculated by equation (3.4). This value also was compared to the spot size of (1.8 ± 0.1) μm measured using the knife-edge technique in which the radius of the beam was determined by measuring the transmitted power while scanning the beam spatially along the x-direction.

Estimation of the standard error was based on measuring the diameter of the ablated area in different directions and finding the mean value of standard deviation.

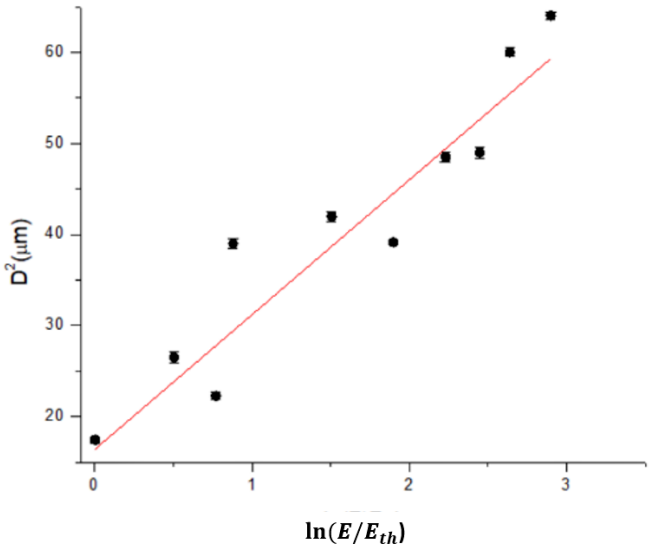

Figure 3.2: The square of the external diameter of a single pulse annular as a function of pulse energy.

The optical vortex beam (OV) is distinguished from Gaussian beam by the zero intensity in the center carrying a topological charge of ℓ that leads to energy

flows within the annular ring, but not at the center opposite to the Gaussian beam, so the fluence for an OV beam is given by [56, 54]:

$$F_{OV}(r) \;=\; \frac{4 \mid \ell \mid Er^2}{\pi\ w_0^4}\ exp\ \left(\frac{-2r^2}{w_0^2}\right). \tag{3.6}$$

Unlike the Gaussian beams, the intensity of the optical vortex beam reduces to $1/e^2$ of the maximum value at two different places on each side of the peak intensity which are at the internal radius (R_{in}) and the external radius (R_{ex}) of the ablated region as shown in figure 3.3. The maximum fluence is limited between the two points at each side of the peak intensity and it occurs at a circle of radius of $r_p = \sqrt{\frac{|\ell|}{2}} w_0$ from the zero intensity center, by substituting the value of r_p in the optical vortex beam fluence equation (3.6) we obtained:

$$F_{\ell,Peak}(r_p) \;=\; \frac{2E\ \ \mid \ell \mid}{\pi\ w_0^2}\ exp\ [- \mid \ell \mid]. \tag{3.7}$$

For example, the peak fluence of the first and second order OV beams that we studied in this work are given by:

For $\ell = 1$,

$$F_{\ell=1,Peak}(r) = \frac{0.74\ E}{\pi\ w_0^2}. \tag{3.8}$$

For ℓ =2,

$$F_{\ell=2,Peak}(r) = \frac{0.54\ E}{\pi\ w_0^2}. \tag{3.9}$$

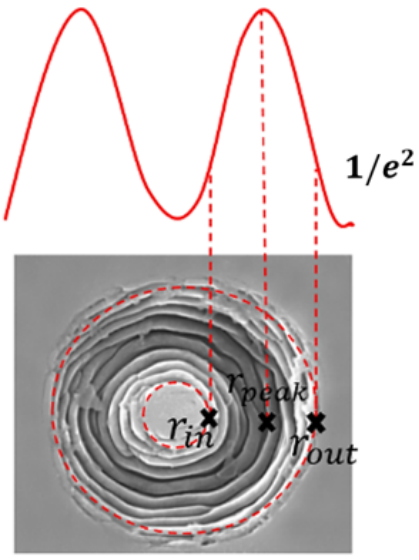

Figure 3.3: The internal and external radii of the ablated area and the point where the fluence is the maximum.

For the micro-structures induced by OV beams, a similar method as in the case with the nano-structures induced by Gaussian beam was implemented to measure the fluence threshold and beam spot size. A single shot experiment was carried out on CVD single crystal diamond at various pulse energies to find the fluence threshold. By measuring the inner radius and outer radius then subtracting the internal radius from the external radius, we obtained the $\sim 6.1\ J/cm^2$ after dividing the pulse energy by the area of the ablated region.

Spot size is obtained by applying the linear fit according to the relation (3.10) [56] on the experimental data points as shown in figure 3.4 3.4, the beam waist was obtained, and it was found to be $(2.13 \pm\ 0.51)\mu m$.

$$w_0 = \sqrt{\frac{(R_{ex}^2 - R_{in}^2)}{\ell \left(\ln \frac{R_{ex}}{R_{in}}\right)}}. \tag{3.10}$$

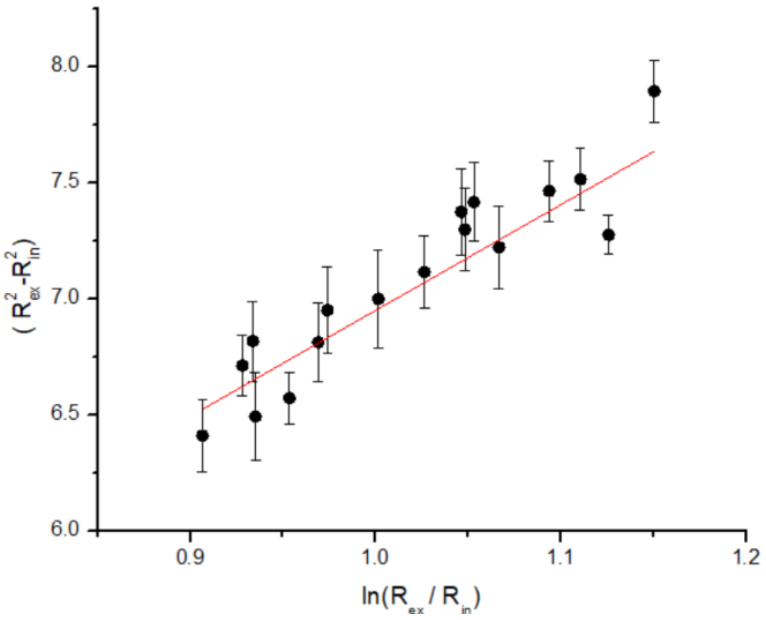

Figure 3.4: Measurement of the beam waist of OV beam.

3.4 Sample

The micro-structures were generated on two different types of single crystal diamond shown in figure 3.5 with dimensions of 3×3 mm and thickness of 0.3 mm, having $<100>$ orientation, purchased from Element Six company. The first type in figure 3.5(a) is grown by high-pressure high-temperature (HPHT) process and doped with nitrogen which gives the diamond yellow color. The second type shown in figure 3.5(b) is fabricated by chemical vapour deposition (CVD) synthesis process. The average roughness of the polished surface is less than 30 nm [2]. Before experiments, the samples were cleaned in methanol or acetone using ultrasonic device for 15 to 30 minutes to remove any dust. This step is repeated after laser ablation to remove any debris deposited on the sample surface due to the ejection of the material such as splashes in the form of nano-droplets during the ablation processes.

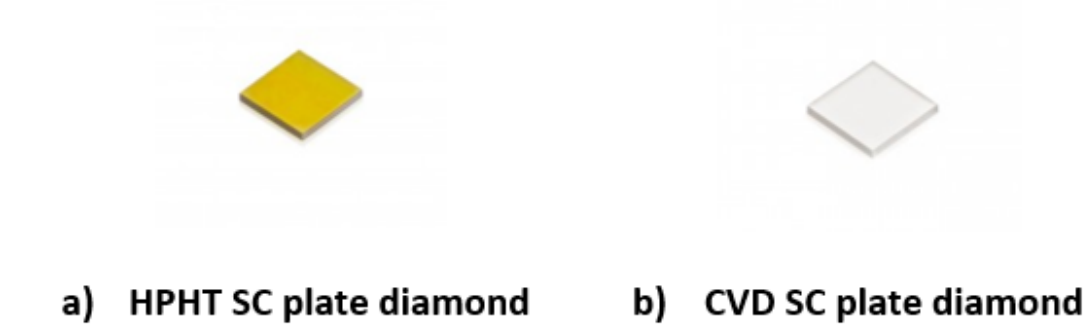

Figure 3.5: Synthesis single crystal diamond plates.

3.5 Experimental setup

3.5.1 Gaussian beams experiment

To determine the threshold fluence, the diamond sample was irradiated with a Gaussian beam in a single pulse mode and pulse energy was varied in small increments. The pulse energies employed on the sample surface were within the range of 10 nJ

to 290 nJ with a pulse duration of 45 fs. To induce periodic nano-structures in our experiment, we used a variable number of pulses ranging from 100 to 1000. By operating the laser in gated mode, the number of pulses irradiating the sample would be varied. The experiments involved irradiating the sample surface with linearly and circularly polarized Gaussian laser beam, separately.

As shown in figure 3.6, the output Gaussian beam generated from the laser amplifier passes through the beam splitter (BS) which reflects a small portion of the beam into the autocorrelator to measure the pulse duration and the rest of the beam passes through. The beam power is controlled by a combination of half-wave plate placed in a digitally controlled rotation stage and the polarization beam splitter. In addition, different neutral density filters were placed within the optical path to further control the incident laser pulse energy. To alter the polarization state of light, a quarter-wave plate used to convert an incident linearly polarized input beam into a left and right circular polarized beam. After the change of polarization, the beam was directed into a 0.25 NA (numerical aperture) microscopic objective lens that focuses the beam normally onto the diamond surface which was placed on a three-axis translation stage (XYZ). The XYZ stage was controlled by a computer and has a precision of 50 nm alongside the x and y directions and 100 nm along the z direction. In order to find the sample surface accurately, the back-reflected light from the sample passing through the microscopic objective lens was directed into the CCD camera. In addition, a collection of neutral density filters have been positioned in front of the camera to ensure that the focused light intensity is below the camera's damage threshold. The surface was determined at very low energy of the incident beam to avoid damage to the camera.

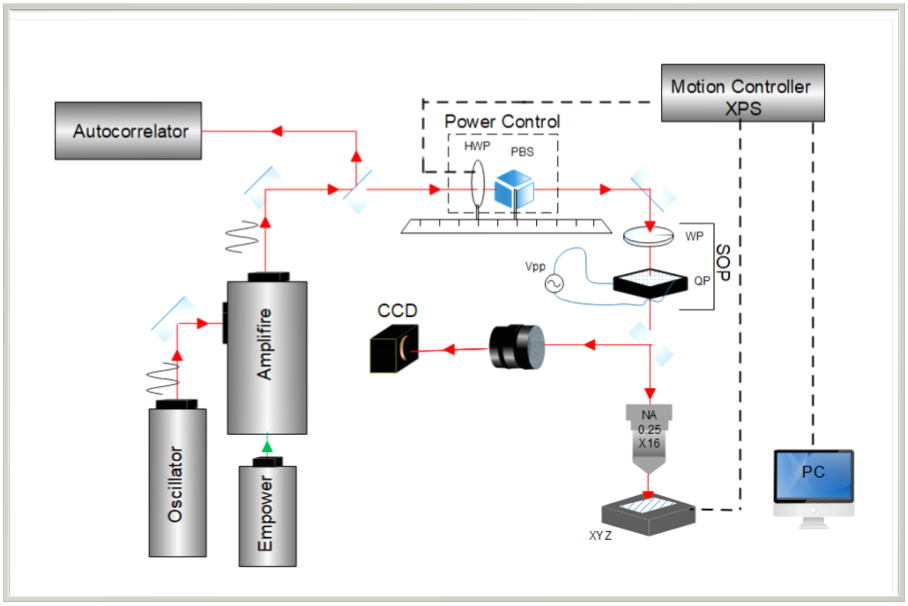

Figure 3.6: Schematic of the experimental setup

3.5.2 Higher-order Gaussian and superposition beams experiment

Complex periodic nano-structures patterns that were generated experimentally by either **pure vector vortex (VV) beams or superimposed vortex beams** were produced by the birefringent liquid crystal plate with a topological charge q at its center defect, (QP). The q-plate is an optical device that converts incident beams with defined spin angular momentum into scalar or vector vortex beam with well defined orbital angular momentum depending on the input polarization of Gaussian beam.

- **Working of Q-plate**

  When a light beam passes through a q-plate, the topological charge ($2q$) is transferred into the phase of the incident beam, which gains a $2q$ amount of OAM, with a sign determined by the input light polarization irrespective of the topological charge q. The q-plate is also characterized by its optical

retardation factor (δ), which governs the SAM to OAM coupling efficiency of q-plate. The action of the q-plate on the input Gaussian polarization can be described by the following formula in which the input polarization is considered in the circular polarization basis [47].

$$E_{out} = \ cos\ \frac{\delta}{2}\begin{pmatrix} e_L \\ e_R \end{pmatrix} + isin\frac{\delta}{2}\begin{pmatrix} e_R\ e^{+2i(q\varphi\ +\ \alpha_0)} \\ e_L\ e^{-2i(q\varphi+\alpha_0)} \end{pmatrix}, \tag{3.11}$$

where φ is the azimuthal angle in the beam transverse plane, and α_0 specifies the initial molecular orientation of the liquid crystals (molecular director). The purity (SAM to OAM coupling efficiency) of the output vortex beam is decided according to the amount of retardation by the q-plate. At an optimal voltage, the δ of the q-plate is equal to π and q-plate is said to be in a tuned state, leading to a full conversion of the incident Gaussian beam into a vortex beam. On the contrary, when $\delta \ \neq \ \pi$, the q-plate is said to be in a detuned state and the output beam contains a partially converted Gaussian beam into a vortex beam and part of Gaussian, i.e., in a superposition state. Thus, the superposition state of a beam consists of different amounts of Gaussian and non-Gaussian beams depending upon the value of δ as governed by the above equation. The optimal voltage was determined experimentally by changing the voltage while monitoring the intensity profile of the beam on an IR card. We noticed that at a specific voltage ($V_{Gaussain}$ is the voltage at which we get a Gaussian beam) the singularity, i.e., null-intensity at the center, of the vortex beam is vanished, so there is no conversion of Gaussian beam. By increasing the voltage, the singularity starts to emerge until we get the null intensity at the center with equal intensity around the singularity in the ring-shaped profile. Knowing the optimal voltage and $V_{Gaussain}$, the relative ratio of the two beams can be easily calculated.

- **Polarization patterns produced by q=+1/2**

  The first configuration in the experiment was to generate periodic patterns based on different polarization states of first-order vector vortex beams using a q-plate with $q = +1/2$ topological charges. Alignment of the q-plate was done to make sure that the singularity is exactly at the center of the intensity beam profile. Linear polarized beams incident on a tuned q-plate with a topological charge of $q = +1/2$ results in radially, azimuthally, clockwise spiral and anti-clockwise spiral polarization patterns of vortex beam that were imprinted in the form of periodic nano-structures on the sample surface by irradiating the sample with multiple pulses at different energies. Also, first-order anti-radial polarization state was generated with a topological charge of $q = +1/2$ on the q-plate (radial) followed by a HWP. Therefore, the HWP was used to reverse the handedness of the spin angular momentum of the vector vortex beam.

- **Polarization patterns produced by q= -1**

  In the second experiment, second-order vector vortex beams were generated by q-plate with -1 topological charge. Two different patterns based on different polarization patterns of vector vortex beams carrying OAM of $\ell = \pm 2$; the first pattern was generated by an input of linearly polarized beam to q-plate with $q = -1$ and the second pattern was produced using configuration with input linear Gaussian beam passing through $q = -1$ followed by a half-wave plate.

- **Polarization patterns of superposition beams**

  For the superposition experiments consisting of Gaussian and vector vortex beams of first and second orders, the q-plates were detuned separately depending upon the desired complex output polarization state of superimposed

beam. For a q-plate with $q = +1/2$, the superposition state of linear Gaussian beam and first-order vector vortex beam produces OAM value of $\ell = 0, \pm 1$. Similarly, a q-plate with $q = -1$ results in OAM with $\ell = 0, \pm 2$.

Finally, complex polarization patterns such as flower-like patterns were produced by using both q-plates, thereby obtaining desired polarization patterns produced by the superposition of 1^{st} and 2^{nd} order vortex beams, superposition of 2^{nd} order vortex beams with polarization selection and superposition of 2^{nd} and 3^{rd} order vortex beams. The following table shows in detail all the configuration used in this work and the corresponding out-put polarization patterns with its OAM values.

Table 3.2: The configuration of generating higher-order Gaussian beams

Configuration	**Out-put beam**	**OAM value**
H-linearly polarized beam $\rightarrow q = +\frac{\mathbf{1}}{\mathbf{2}}$	Radial	$\ell = \pm 1$
V-linearly polarized beam $\rightarrow q = +\frac{\mathbf{1}}{\mathbf{2}}$	Azimuthal	$\ell = \pm 1$
D and A-linearly polarized beam $\rightarrow q = +\frac{\mathbf{1}}{\mathbf{2}}$	Clockwise and anti-clockwise spiral	$\ell = \pm 1$
H-linearly polarized beam $\rightarrow q = +\frac{\mathbf{1}}{\mathbf{2}}$ followed by HWP	Anti-radial	$\ell = \pm 1$
H-linearly polarized beam $\rightarrow q = \mathbf{-1}$	Type-II	$\ell = \pm 2$
H-linearly polarized beam $\rightarrow q = \mathbf{-1}$ followed by HWP	Type-I	$\ell = \pm 2$
H,V,D or A-linearly polarized beam $\rightarrow$ detuned $q = +\frac{\mathbf{1}}{\mathbf{2}}$	Superposition of Gaussian and 1^{st} order vortex beam (Crescent-shaped patterns)	$\ell = 0, \pm 1$
H-linearly polarized beam $\rightarrow$ detuned $q = \mathbf{-1}$	Superposition of Gaussian and 2^{nd} order vortex beam	$\ell = 0, \pm 2$
H-polarization $\rightarrow q = -1 \rightarrow$ HWP $\rightarrow q = +1/2$	A three-petal flower-like structure	$\ell = \pm 1, \pm 2$
H-polarization $\rightarrow q = -1 \rightarrow$ polarizer	A four-petal flower-like structure	$\ell = 0, \pm 2$
H-polarization $\rightarrow q = -1 \rightarrow q = +1/2$	A five-petal flower-like structure	$\ell = \pm 2, \pm 3$

- Horizontal (H), Vertical (V), Diagonal (D), and Anti-diagonal (A).

3.6 Characterization of laser modified regions

Scanning electron microscope (SEM) was used to analyze and characterize the ablated area on the sample surface. The SEM operates by scanning the sample surface with an electron beam. After cleaning the sample in methanol or acetone for approximately 15 minutes, the samples were coated with 10 nm of gold to avoid any charging effect that minimizes the image resolution. The SEM images were obtained after scanning the sample surface linearly by a low accelerated voltage electron beam

of 5 keV and the generation of secondary electrons that are collected into the detector.

Chapter 4

Experimental visualization of complex polarization states of light

This section describes experimental visualization of different complex polarization states of light in the form of nano-structures generated by Gaussian, pure vector vortex and superimposed beams. It includes different models to explain the physics behind the nano-ripple structures formation and analysis of their periodicity.

4.1 Periodic surface structures

When multiple laser pulses irradiate diamond surface, it gives rise to the formation of LIPSS (laser-induced periodic surface structures) which gives a feasible way towards control of material surface properties such as the optical, chemical and mechanical properties for industrial applications. We relied on these structures (nano-ripples) to visualize the polarization states of light because the orientation of such structures depends on the laser polarization. In the past studies, the fabrication of nano-ripples was observed on the surface and inside a solid. Indeed, the direction of the ripples

was reported either parallel [57] or perpendicular to the beam's electric field [58].

Different models were introduced to explain the formation of LIPSS. In [59] the periodic structures observed inside silica glass after direct femtosecond writing process were explained in term of nano-plasmonic model. An alternate mechanism of grating formation was also proposed that involves interference between the incident light and the electron plasma wave [59]. It is predicted that the periodicity depends on the electron plasma temperature ($T_e \sim 10^7 k$) and the electron density ($N_e \sim 1.75 \times 10^{21} cm^{-3}$). However, in the current experiment, the pulse energy deposited into the modified region is inadequate to fulfill even close to $10^7 k$. To reach to an electron temperature of $T_e \sim 10^7 k$, the pulse energy of $\sim 11 \mu J$ should be applied. Whereas the pulse energies that were used in this work to form the nano-structures are of few hundreds of nanojoules. Therefore, the low threshold conforms with the plasmonic model in which the electron temperature is restricted by the electron-ion collisions to the order of material bandgap. In this model, the periodic self-organized nanograting like structures of $(170 \pm 25)\ nm$ width are aligned parallel to the laser polarization direction [60].

Nano-plasmonic model proposed that the light-plasma interaction followed by local field enhancement and self-organization is the cause of nano-ripples formation. It can be explained as follows: when the light is directed and being focused onto the surface of the sample, the nonlinear absorption occurs. The first pulse comes and then the ionization takes place in random spots. It is random because any materials are most likely to have some defects or impurities such as color centers. Since the energy of the incident pulse is high enough, half of the pulse is ionizing the material, so creating the plasma and the rest of the pulse is interacting with the formed plasma. When the second pulse comes, these ionized regions get more ionized due to incubation effect and over a few number of pulses, spherical nanoplasmas are created within the focal volume but still in random places. Over thousand of laser pulses,

those random nanoplasmas develop into nanoplanes due to local field enhancement. Assume having spherical plasma and the electric field is along the direction indicated in the schematic figure 4.1. If the plasma density is greater than the critical density, the plasma behaves as metal-like nano-particles in which the electrons are collectively oscillating back and forth. Due to collective motion of electrons, the electric field gets redistributed around a nano-particle, resulting in higher intensity at the poles than at the equators. As a result, a spherical nanoplasma becomes elongated along the field direction.

For metal nano-particles, $\varepsilon > 1$ where ε is the permittivity, therefore the field is higher at the poles than at the equators as shown from the equations in the schematic figure 4.1. So the circular nanoplasmas grow as elliptical plasma along the laser polarization. If the light is being focused inside the material, local field enhancement causes the spherical plasma to elongate perpendicular to the polarization direction since the plasma density will be below the critical density, the plasma is underdense and the field enhancement is along the equators.

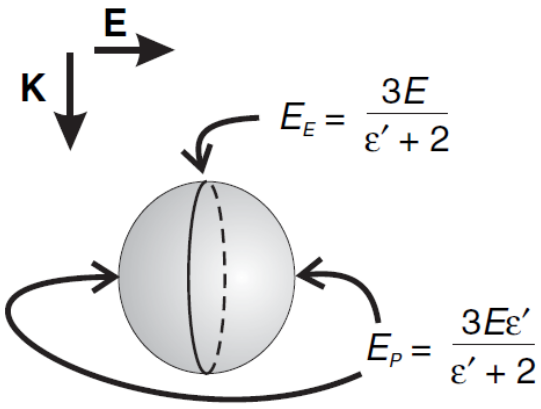

Figure 4.1: A schematic illustrates local field enhancement outside nanoplasma. **K and E** are the laser propagation direction and the electric field, respectively. E_E is the local electric field found at the equators and E_P is the local field at the poles. ε is the ratio of permittivities of nanoplasma and dielectric medium [60].

As the nanoplasmas are developed and grow to the size of the light wavelength, hence leading to quasi-metallic waveguiding, the self-organization takes place be-

cause the light will only reinforce those that are exactly half of the light wavelength. This leads to the minimum spacing to be $(\frac{\lambda}{2n})$, where n is the refractive index of the media.

In this work, LIPSS with a period as small as a few tens of nanometers were recorded on diamond surface using ultrashort laser pulse in multipulse regime. As a result of light-matter interaction, different structures of a light polarization including simple polarization states such as linear of Gaussian beams, patterns like radial and azimuthal belonging to optical vortex beams, and complex polarization states such as flower-like pattern were mapped on diamond surface in a form of self-oriented periodic grating-like structures (ripples) aligned along the direction of laser polarization.

4.1.1 Periodic surface structures produced by Gaussian beam

We investigated the periodic surface structures at various pulse energies, number of pulses and different polarization states of Gaussian beams. Since the formation of LIPSS was the core aim of this work, we carried out all the experiments in multipulse regime. Our work primarily consists of periodic nano-surface structures which were formed with multiple laser pulses (more than 5 pulses) and was recorded upon irradiating the target surface with different varying pulse energies ranging from 10 nJ to 290 nJ and with variable number of pulses ranging from (100 to 1000). Following figure presents the interaction of linearly polarized beam with energies above the energy threshold as shown in figure 4.2.

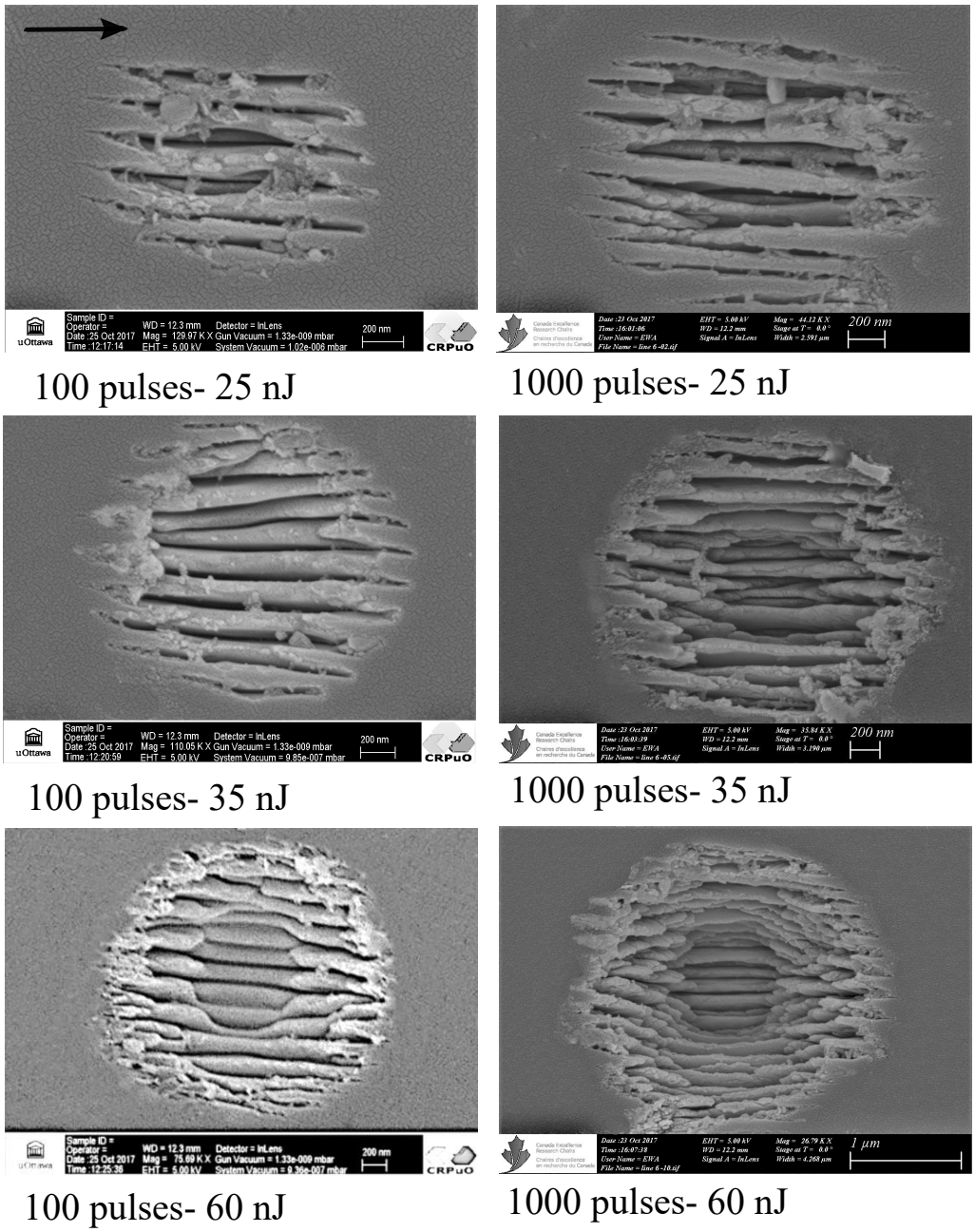

Figure 4.2: Set of SEM images of modified regions generated with 100 and 1000 pulses, pulses energies as indicated in the image and the polarization is indicated with the solid black arrow.

Moreover, nano-structures formed by focusing left and right circularly polarized light on diamond surface at energies above the energy threshold and multiple pulses of 100 and 1000 are shown in figures 4.3 and 4.4, respectively.

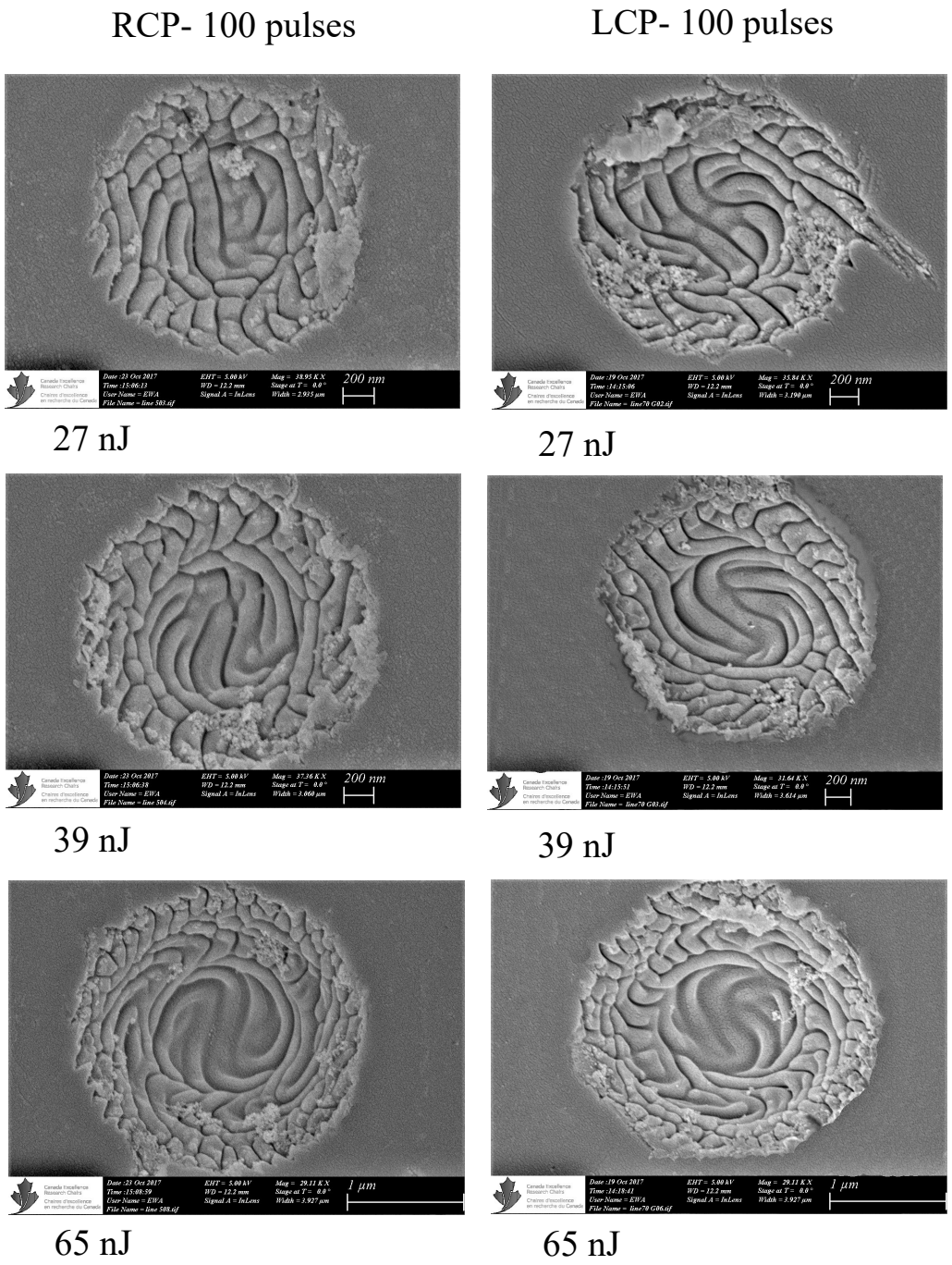

Figure 4.3: SEM images of nanoripples generated via right circular polarization (RCP) and left circular polarization (LCP) with 100 pulses.

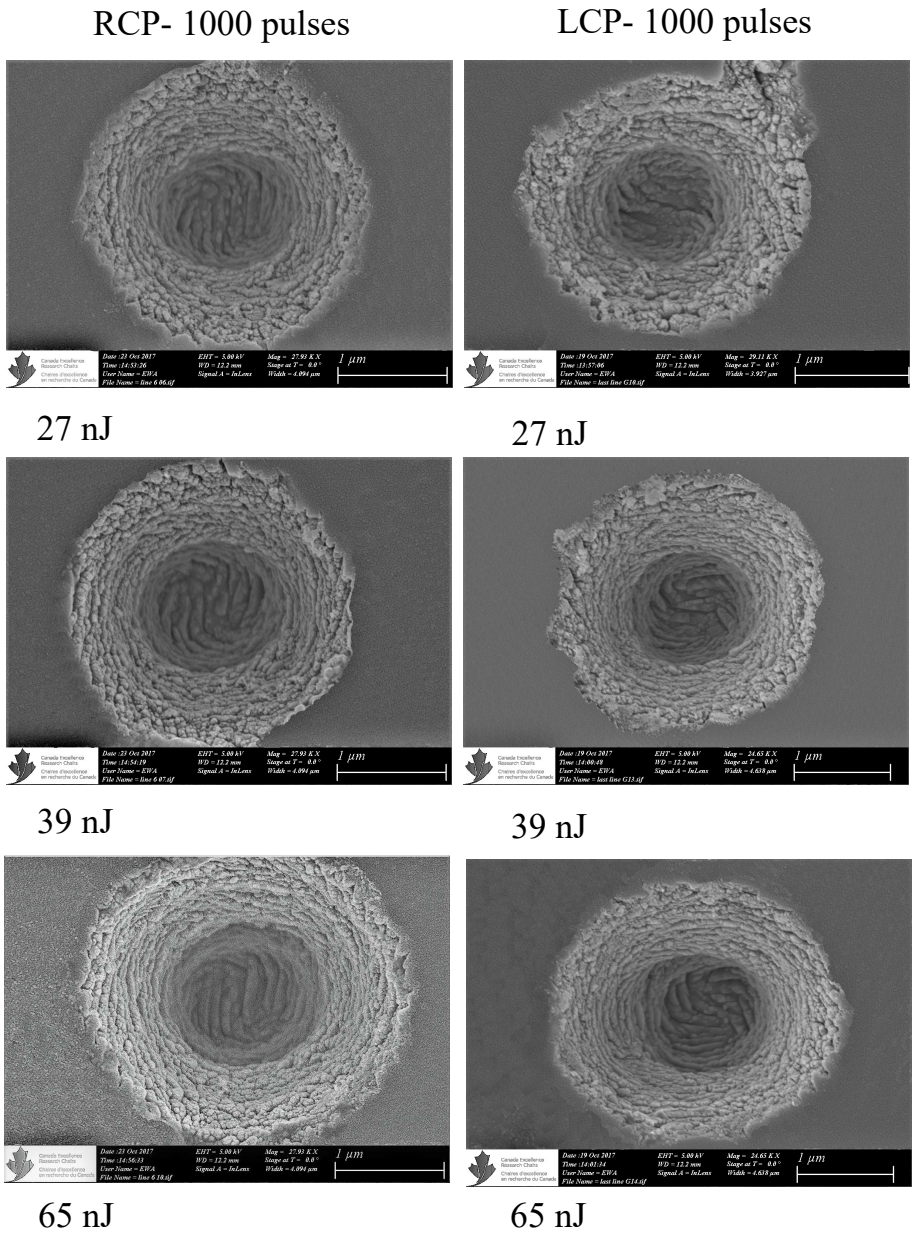

Figure 4.4: Set of SEM images of diamond ablated area using right and left circular Gaussian beams with 1000 pulses.

Simple polarization pattern such as circular and linear Gaussian, was mapped on diamond surface. According to the above figures, the surface morphology attained over multiple pulses (usually greater than 5 pulses per spot) provides a direct visualization tool of the polarization patterns of the incident beam. The nano-ripples generated in figures 4.2 and 4.3 represent linear Gaussian and circular Gaussian

beams, respectively. It can be noticed that the middle of the ablated area is deeper than the outer edge due to the intensity profile of Gaussian beam. They were formed at pulse energy slightly above the ablation threshold at which material removal is initiated. The single pulse threshold of $\sim$ 4.9 J/cm^2 for single crystal diamond is consistent with the threshold value of 4 J/cm^2 recorded by Ramanathan et al. [61] using 200 fs pulses. Thus, finding the threshold ablation is crucial to avoid the formation of debris and deep hole because of the high energy accumulated into the media.

4.1.2 Periodic surface structures produced by different orders of vector vortex and superposition beams

In this work, a direct visualization of complex polarization state of light was achieved in a form of periodic grating-like structures formed within the ablation craters. We demonstrated an uncomplicated method for visualization of complex polarization state of higher-order vortex beams as well as their superposition states by permanently imprinting the polarization states of such beams on diamond surface in a form of periodic grating-like structures (ripples).

- **First and second order vector vortex beams**

  The observation of various polarization states of first and second order vortex beams generated based on q-plates with topological charge of +1/2 and -1 are presented. By optimally tuning the q-plate with $q = +1/2$ electrically, the four cases of linearly Gaussian beam, which are (H (horizontal), V(vertical), D (diagonal), A (anti-diagonal)), were reconstructed into radial, azimuthal, spiral and anti-spiral polarization as shown in figures 4.5, 4.6, and 4.7, respectively. In addition to the anti-radial polarization state of light (equatorially diagonal polarization represented by Poincaré sphere of order $\ell = -1$) which can be

generated by flipping the polarity of the output beam using HWP shown in figure 4.8. The nano-structures produced by first order vortex beams were obtained by irradiating the diamond surface with variable number of pulses ranging from 50 to 500 pulses with varying the pulse energies from $\sim$ 260 nJ to 380 nJ. Results precisely mimicked the beam electrical field distribution as they are in agreement with the simulated results presented in the same figures which were simulated in Matlab by considering the LG beam equation in circular basis and considering the Jones matrix element of the optical devises used. We used the quiver function to plot the vectors, i.e, both the circular components in polar basis.

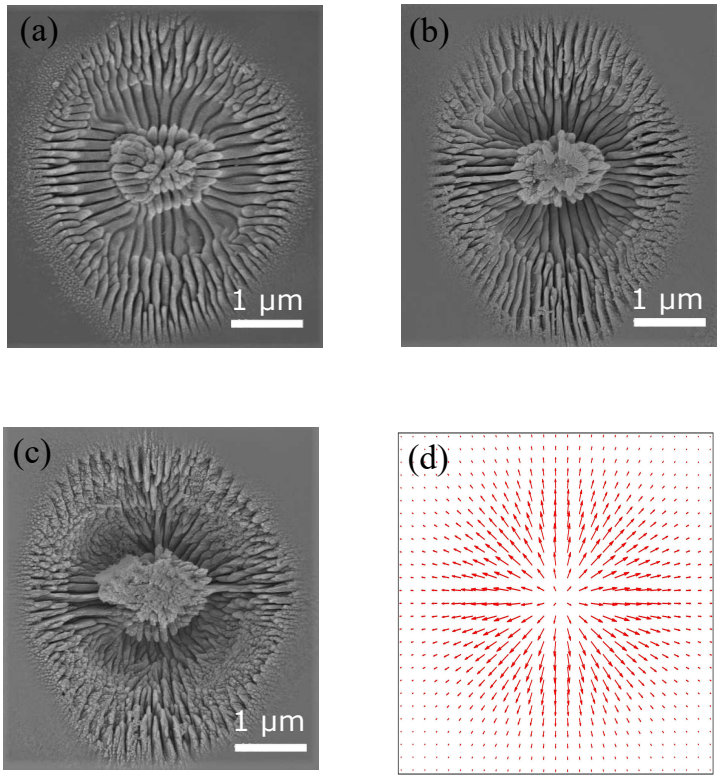

Figure 4.5: SEM images of periodic nano-structures showing the mapping of radial polarization state of light on diamond surface. a) 100 pulses, b) 250 pulses and c) 500 pulse irradiated the sample with an energy of 310 nJ. d) shows the expected polarization pattern [1].

[1]The arrows in figure 4.5(d) represent the instantaneous simulated electric field direction and in theory we cannot predict which way electric field is directed, therefore arrows should be double headed in mutually opposite directions.

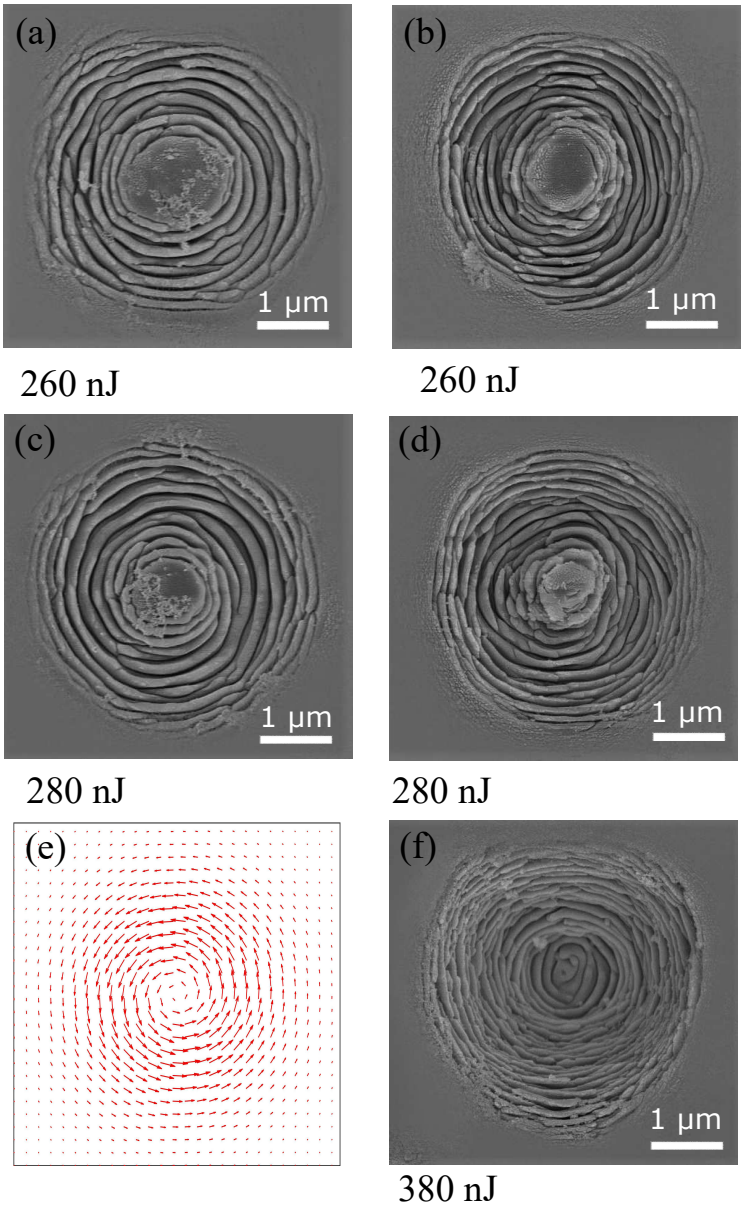

Figure 4.6: SEM images of periodic nano-ripple structure on diamond surface after irradiating it with azimuthal polarization state of first-order VV beam with 100 pulses (a, c) and 250 pulses (b, d, f). e) is the simulated azimuthal pattern.

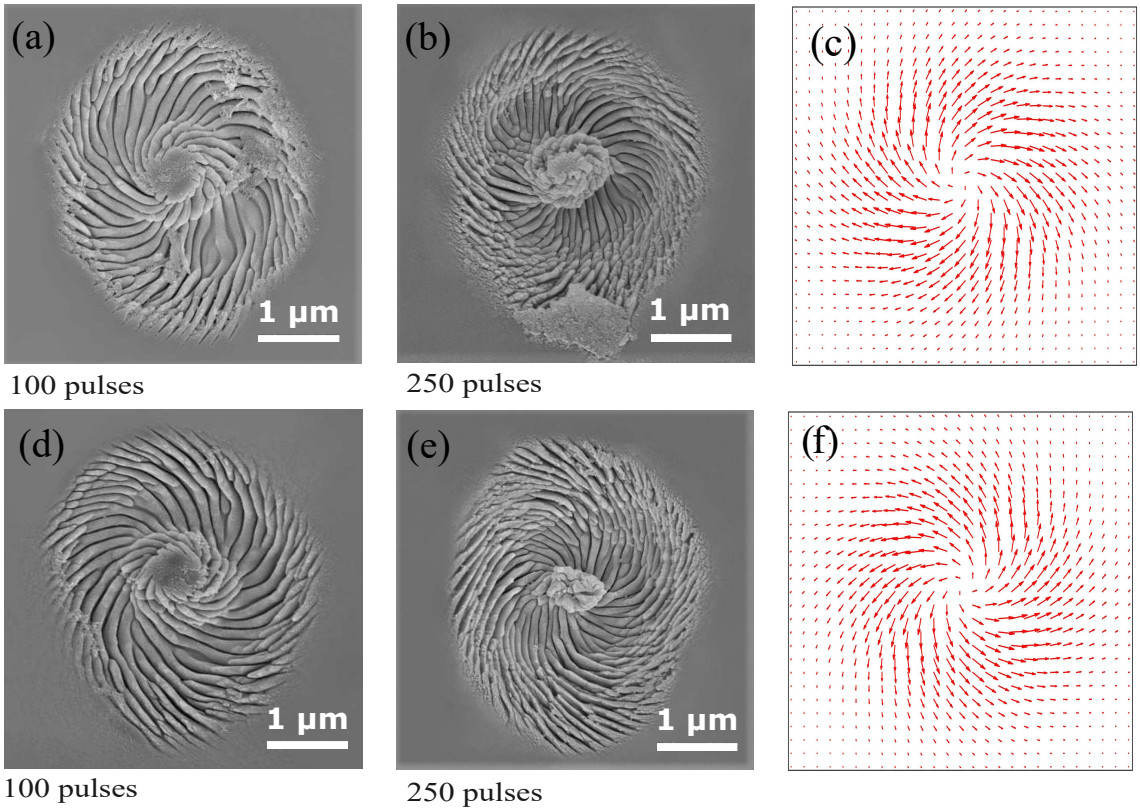

Figure 4.7: SEM images of periodic nano-ripple structure on diamond surface after irradiation of (a,b,c) clockwise spiral and (d,e,f) anti-clockwise polarization state of first-order vortex beam with energy of 310 nJ.

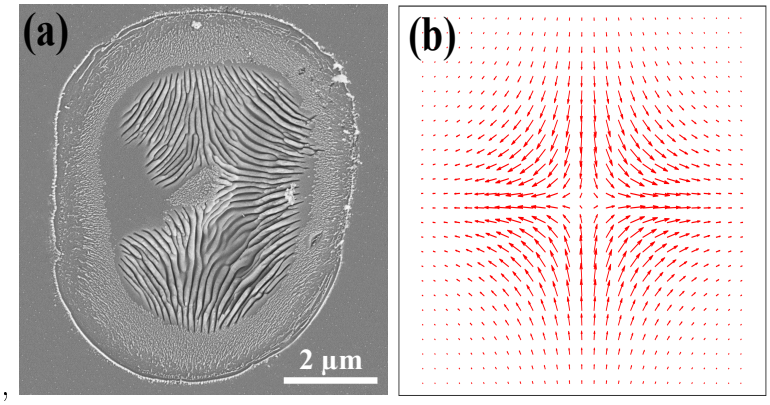

Figure 4.8: A SEM image shows mapping of a) anti-radial polarization state of first-order vortex beam on diamond surface with 100 pulses and corresponding energy of 310 nJ per pulse and b) corresponding simulated polarization patterns.

The polarization pattern of second-order vortex beams which is generated by the tuned q-plate with a topological charge of -1 having linear Gaussian beam

as input, mapped on a solid as shown in figures 4.9 and 4.10 for two different polarization states of 2^{nd} order vector vortex beams. The self-organized periodic nano-structures shown in figures 4.9 and 4.10 were formed after irradiating the diamond surface with multiple number of pulses of 50, 100 and 250 pulses having pulse energy of 400 nJ.

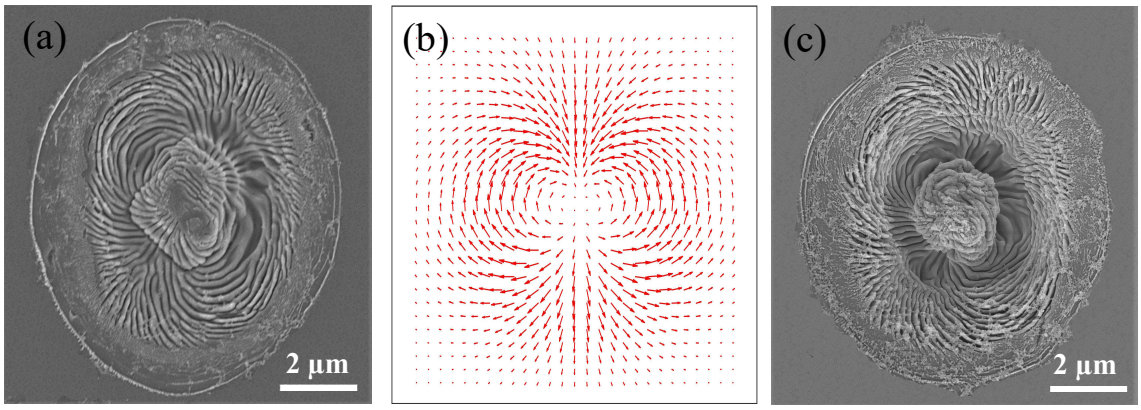

Figure 4.9: SEM images of periodic nano-ripples formed by type-I polarization state of second-order vortex beam with a) 100 pulses and c) 250 pulses with an energy 400 nJ.

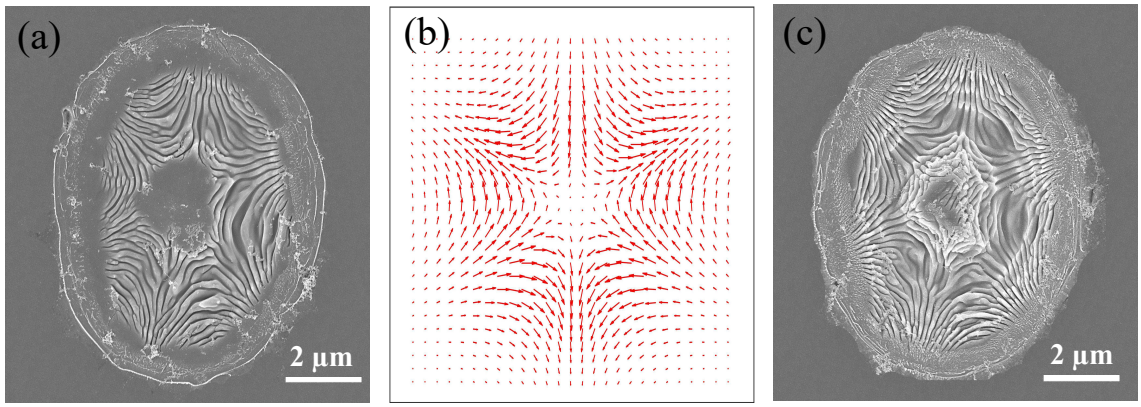

Figure 4.10: SEM images of periodic nano-structures formed by type-II polarization state of second-order vortex beam with a) 50 pulses and c) 100 pulses with an energy 400 nJ.

Based on q-plate, variety of unconventional polarization structures were printed on diamond surface through femtosecond laser-writing technique using energy close to the ablation threshold which is $\sim 6.1 J/cm^2$. Figures (4.5, 4.6, 4.7,and

4.8) represent radial, azimuthal, spiral, anti-radial polarization patterns in the form of periodic nano-grating structures, respectively. These nano-structures were generated by adjusting the axis of the input beam to H, V, D, A with respect to the axis of the q-plate with topological charge of $q = +1/2$. Unlike the others, the anti-radial shape (mapped on a Poincaré sphere represented for $\ell = -1$) was generated by flipping the handedness of the output beam of q-plate ($q = +1/2$) using HWP, corresponding to the same star-like shape generated by q-plate with $q = -1/2$. The formed nano-structures are accurately mimicking the structures of the electrical field of the beam as can be confirmed by comparing with the simulated results in the same figures. The polarization pattern of second-order vortex beams as shown in figures 4.9 and 4.10 is the output of linear Gaussian beam passing through q-plate with topological charge of -1.

The unaltered region at the center of the ablated area appears in almost each figure of higher-order Gaussian beams at low pulse energies. The unaffected area is due to the beam cross-section intensity profile which has null-intensity at the center. Yet, increasing the pulse energies or number causes in extending the ripples to slightly cover the unmodified center. When the energy deposited in the media is close to the ablation threshold, either with Gaussian or non-Gaussian beams, the nano-ripples are sharper and clearer, while exceeding the energy deposition leads to wider ripples or in abrupt ablation regions (holes).

- **Superposition beams**

We further extended our experimental profile with superposition between different order beams. Firstly, asymmetrical complex polarization states of light that arise from superposition of different order vortex beams were imprinted on diamond surface. Different ratios of Gaussian and first-order vortex beams

combined to form nano-structures in a form of moon shape as shown in figure 4.11. The outcome of superimposing the two beams (superposition beams) indicates in shifting of the position of singularity to the left as in figure 4.11a, upward as in figure 4.11b, or diagonal as in figure 4.11c toward the outer edge of the ablated craters. Shifting of the singularity in a specific direction is achieved by adding calculated phase to the Gaussian beam incident on the q-plate. The distance between the origin center and the shifted singularity is governed by the amount of conversion of vector vortex beam into Gaussian beam through q-plate. As the ratio of Gaussian beam with respect to the vector vortex beam increases, the distance between the center and the shifted singularity increases. Therefore, we achieved two degrees of freedom, i.e., one in selecting the specific direction of shift in singularity and other is the amount of shift in singularity in a specified direction. The surface was irradiated with multiple laser pulses ranging from 50 to 250 pulses per spot with varying pulse energies to form the ripples that are oriented parallel to the polarization orientation of light, hence reflecting the light polarization distribution.

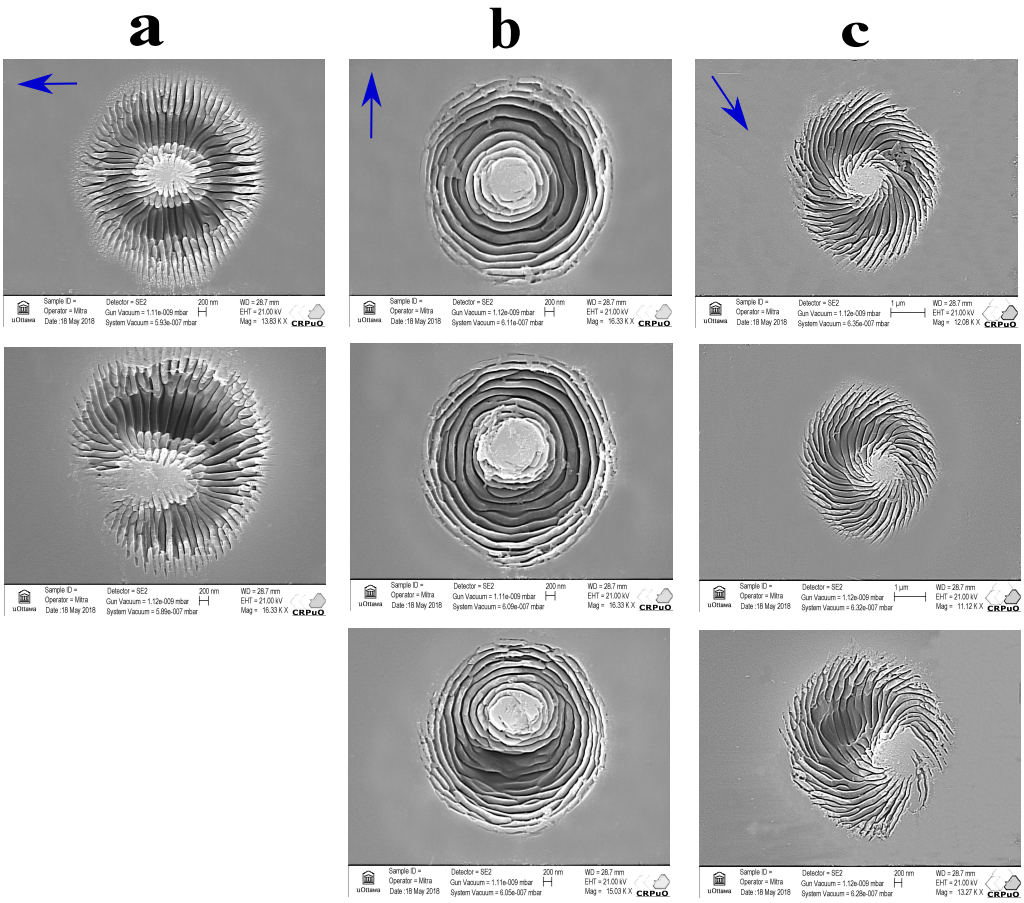

Figure 4.11: SEM images of periodic nano-ripple structures formed via the superposition of linear Gaussian and first-order Gaussian beams for relative weight of (first row) 0:100 (pure VV beam), (second row) 30:70, and (third row)45:55; superposing Gaussian beam with radial beam (first column on the left), azimuthal (second column) and spiral (third column). The direction of shift in singularity is shown with blue arrow on the top left of the image. The nano-structures were formed by irradiating the sample with 100 pulses with a pulse energy of 280 nJ.

Splitting of the singularity into two as in figure 4.12 was observed in case of superposition of second-order vortex beam with Gaussian beam. By detuning the q-late with topological charge of -1, we achieved the superposition of Gaussian beam with second-order vector vortex beams which resulted in two singularities. The distance between the two singularities was controlled by the ratio of Gaussian beam in the superposition of two beams. The following figure presents different superposition ratios.

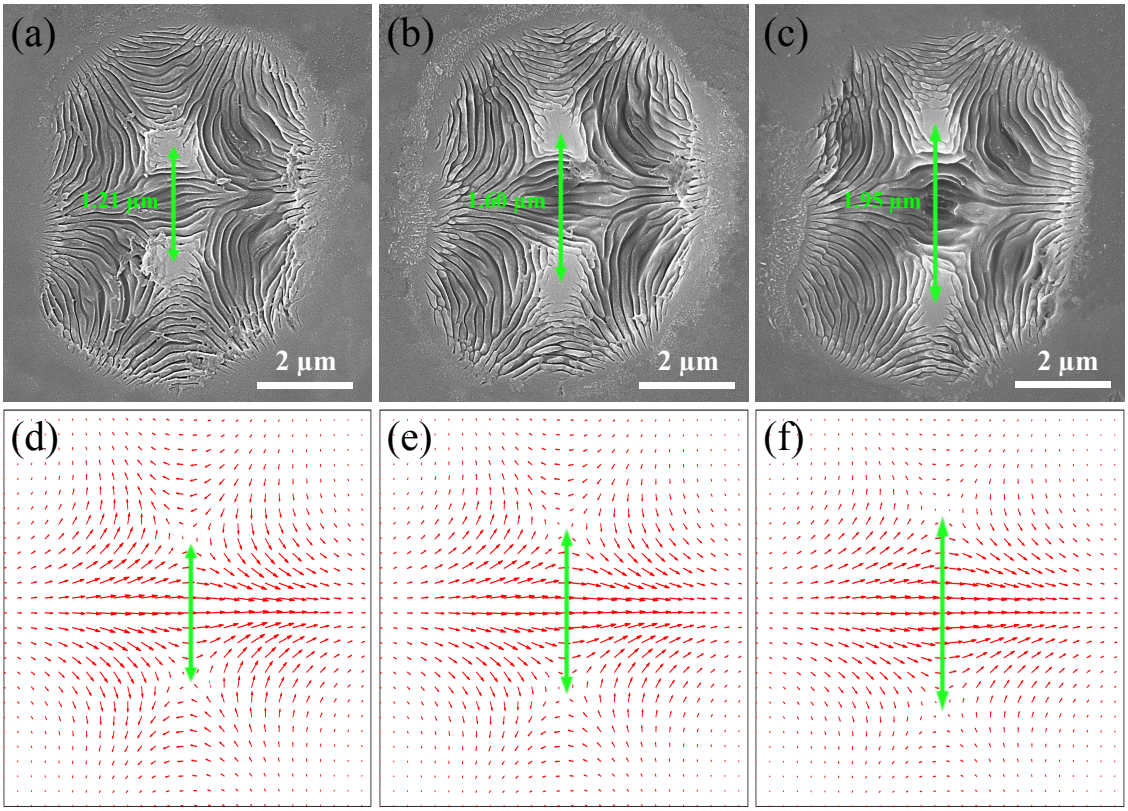

Figure 4.12: SEM images of the periodic nano-ripple structures formed via the superposition of linear Gaussian and second order vector vortex beams with relative weight of (a), (d) 20:80; (b), (e) 30:70; and (c), (f) 40:60. The nano-structures generated by 50 pulses with a pulse energy of 600 nJ.

Reason for splitting and shifting of singularities is attributed to the destructive interference that occurs during the superposition of linear Gaussian and optical vector vortex beams, two waves are out of phase at one point in case of first-order OVV beam and two points in case of second-order OVV beam, hence one and two singularities, respectively. The nano-ripples arrangement is polarization dependent of the vector vortex beam. The distance between the two null-regions rises by increasing the ratio of imposed Gaussian beam on the vector vortex beam.

Further unconventional unique flower-like nano-structures in figure 4.13 formed within the ablated zone are generated by combining two different orders of vector vortex beams. The superposition beams yield in nano-structures with

three, four and five localized regions within the focal volume. First, the three-petal flower-like structure (figure 4.13a) was generated by tuned q-plate with topological charge of -1 and detuned q-plate with topological charge of $+1/2$ with HWP in between. A three-petal flower-like structure beam is expressed mathematically as follows [47]:

The beam after $q = -1$ tuned plate defined by:

$$e^{i2\varphi}\mathbf{e}_{\mathrm{R}} + e^{-i2\varphi}\mathbf{e}_{\mathrm{L}}. \tag{4.1}$$

Then passing through the detuned $q = +1/2$ plate, resulting in a beam defined by:

$$\alpha(e^{i2\varphi}\mathbf{e}_{\mathrm{R}} + e^{-i2\varphi}\mathbf{e}_{\mathrm{L}}) + \beta(e^{i\varphi}\mathbf{e}_{\mathrm{L}} + e^{-i\varphi}\mathbf{e}_{\mathrm{R}}), \tag{4.2}$$

where α and β are the numerical ratios of both beams. The ripples in each petal extended differently along the light electric field of the superimposed beam as shown in the simulated result in figure 4.13b.

Figure 4.13(b) shows the four-petal flower-like structure which was formed by placing a polarizer after the q-plate of -1 topological charge, acting as a polarization selector, i.e., transmitting preferred direction as reflected in the intensity profile of the vector beam. Unlike the three-petal flower-like pattern, the ripples oriented in the same direction in each one of the localized regions because of the polarization selection via polarizer.

Finally, the five-petal flower-like structure was obtained by using a tuned q-plate with topological charge of -1 and detuned q-plate with topological charge of 0.5 as shown in figure 4.13(c) and mathematically defined as:

$$e^{i2\varphi}\mathbf{e}_{\mathrm{R}} + \ e^{-i2\varphi}\mathbf{e}_{\mathrm{L}} = \alpha(e^{i2\varphi}\mathbf{e}_{\mathrm{L}} + e^{-i2\varphi}\mathbf{e}_{\mathrm{R}}) + \beta(e^{i3\varphi}\mathbf{e}_{\mathrm{R}} + e^{-i3\varphi}\mathbf{e}_{\mathrm{L}}). \tag{4.3}$$

The five-petal flower-like nano-structure shown in figure 4.13(c) arose because of conversion of the incident beam according to equation (4.3). The orientation of the nano-ripples at each of the petals is oriented differentially and is a snapshot of the simulated polarization pattern shown in figure 4.13(f).

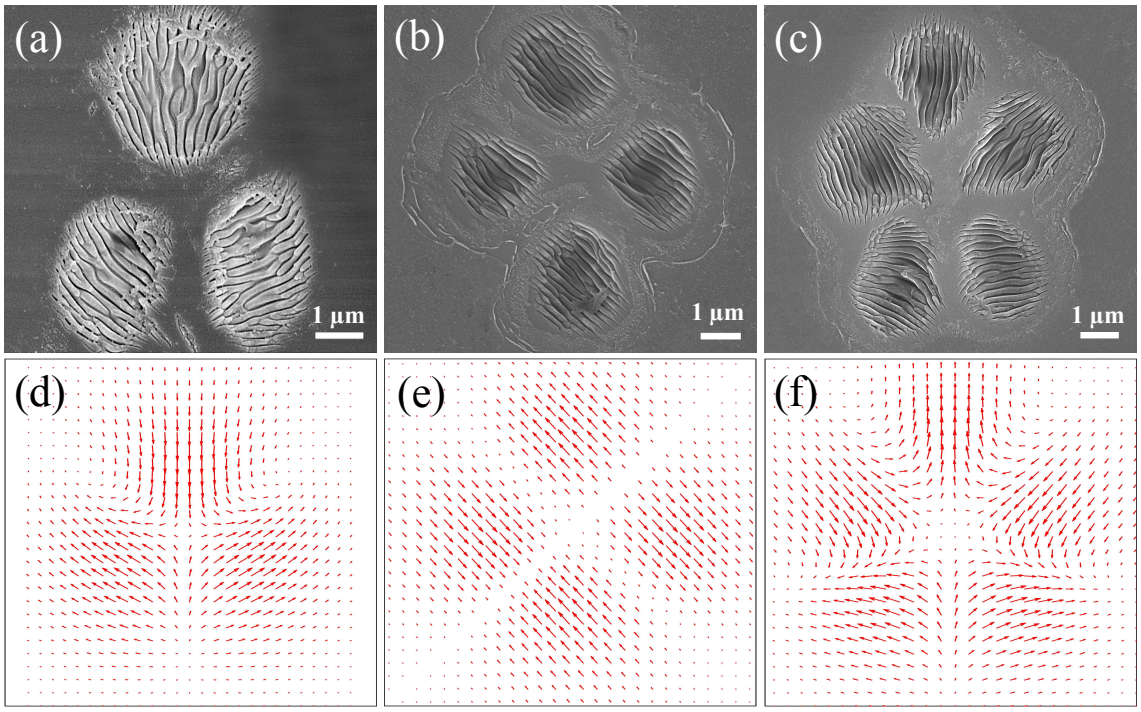

Figure 4.13: SEM images of flower-like patterns formed by a) superpositions of first and second order vector vortex beams, (b) second-order vector vortex beam with selected polarization, and (c) second and third order vector vortex beams. All patterns generated using 50 pulses with energy of 700 nJ. The bottom panels (d,e,f) present the expected polarization pattrens.

4.2 Periodicity of periodic nano-structures

Figures 4.14 and 4.15 show the periodicity of the nano-surface structures obtained by first and second order vortex beams as a function of pulse energies (E) and number of pulses (N), respectively. Based on 2-Dimensional Fast Fourier transforms (2D FFT), ripple periodicity (Λ) is calculated by taking the predominant peak represented in the 2D FFT spectrum. Although, at different numerical values of E and N, consistency in the periodicity was observed. The periodicity obtained experimentally

is 170 $nm \pm 25$ nm which agrees with the theoretical value given by ($\lambda/2n = 166$ nm) where λ is the laser wavelength and n is the material refractive index [60].

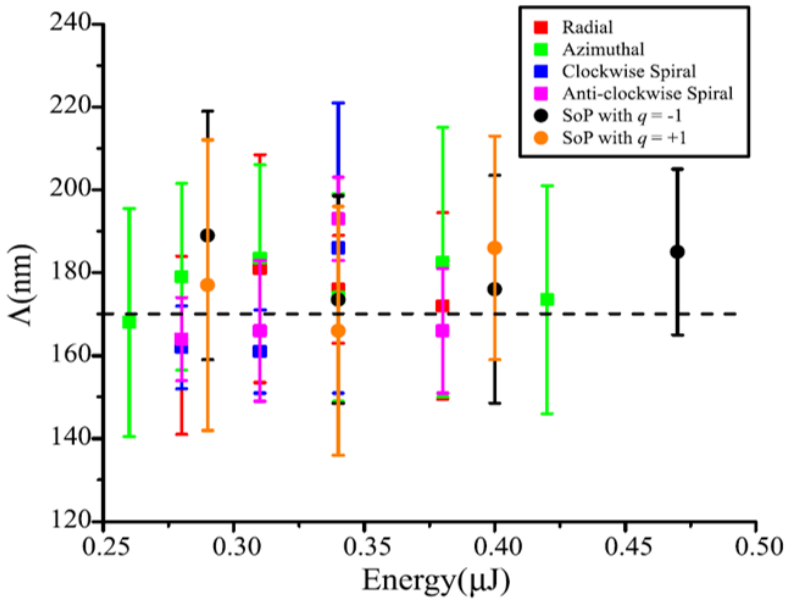

Figure 4.14: The periodicity of periodic nano-ripple structures formed upon the irradiation of first and second order of vortex beams as a function of pulse energies.

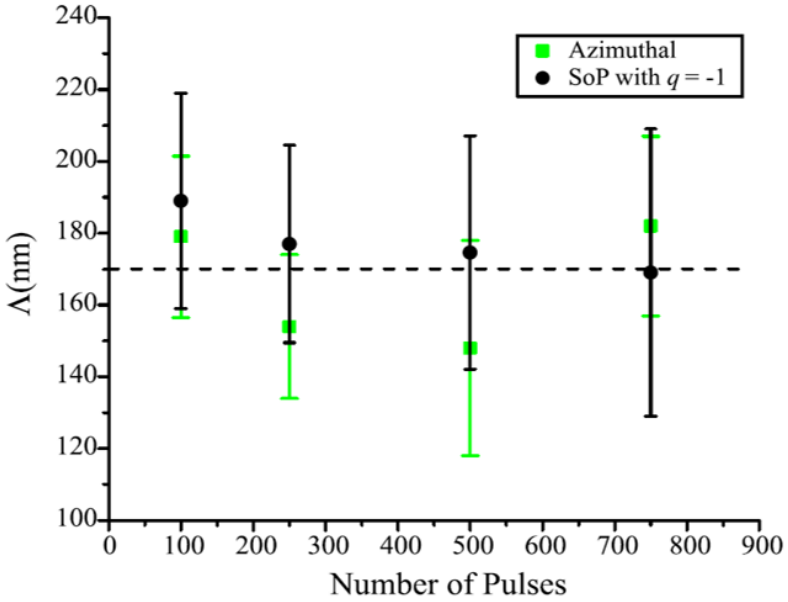

Figure 4.15: Comparison of the periodicity of nano-ripples created from first and second order vortex beam as a function of number of pulses.

Chapter 5

Conclusion and future outlook

5.1 Summary

Further understanding of ultrafast laser-material interaction enabled researchers to achieve material micromachining in a controlled fashion. The control and manipulation of material properties on the micro and nanoscale using ultrafast laser micromachining technique is a promising technology in the field of nano and biophotonics, biomedicine, integrated optics and quantum technologies. Despite the advancement that has been made since the advent of ultrafast laser technology, there is a lot to explore and investigate. For example, the interaction of ultrafast vector vortex beams having complex polarization structures with chiral structures in crystalline as well as in liquid forms is not completely understood.

In this thesis, a set of polarization structures including symmetric and asymmetric patterns were imprinted on synthetic CVD diamond surface via femtosecond laser writing technique. The line-like structures within the focal volume were aligned accurately along the direction of the electrical field. Studying the nanosurface structures in the form of ripples as a function of different number of pulses

with variable pulse energies were fully addressed. We investigated the fabrication of nano-structures using Gaussian, various order of vector vortex and superposition beams. Using multiple-pulses, nano-structures were formed with linear and circularly polarized Gaussian beams. The direction of the ripples generated was parallel to the polarization state of light. In addition, higher-order polarization patterns are imprinted on diamond surface by different order of vector vortex beams.

The polarization prototypes of radial, anti-radial, azimuthal and spiral, etc., beams generated using q-plates with different topological charges were mapped accurately onto the diamond surface. Mapping of the unconventional polarization state of light generated using the superposition of several order optical vector vortex beams, by imposing Gaussian beams onto 1^{st} and 2^{nd} order of optical vector vortex beams was also achieved. In the case of pure optical vector vortex beams, the singularity remains at the center, unmodified. The central singularity shifts toward the outer edge of the ablated area in a specified direction governed by the amount of Gaussian beam in the superposition as well as the polarization direction of linear Gaussian beam. As the amount of Gaussian beam imposed increases, the singularity moves further towards the outer edge, hence its distance increases from the center.

Further, superposing a linear Gaussian with the second-order vector vortex beams causes splitting of the singularity into two. The distance between the two newly generated singularities becomes greater as the amount of vector vortex beam decreases.

Moreover, non-uniform birefringent flower-like patterns with multiple petals and periodic line-like structures aligned differentially in each petal were mapped onto a diamond surface. The different orders of vector vortex beams imposed controlled the number of the localized regions generated. The physics behind the formation

of such nano-ripples that are parallel to the polarization state of light is discussed, owing to the physical phenomena: local field enhancement and self-organization following the nonlinear processes and light-plasma interaction. Resulting in periodic nano-ripples with ripple width of approximately $(170 \pm 25)nm$.

5.2 Future outlook

We mainly focussed upon femtosecond vector beams produced by q-plates with a topological charge of $q = +1/2$ and -1 in several configurations such as (a) tuning q-plate optimally, thereby achieving full conversion of a Gaussian beam into OAM beam and (b) detuning the q-plate, therefore generating superposition beams which can be used to form even more complicated unconventional surface patterns. To the best of our knowledge, micromachining of target surface by accurately mapping the complex polarization state of light related to higher-order vector vortex beams and unconventional polarization patterns generated by superposition beams have not been experimentally achieved. Therefore, the approach used in our work offers a simple fast tool to picture the electric field structures of various beams in the form of LIPSS.

LIPSS can be printed on various material surfaces using a single-step process, which is direct femtosecond laser writing technique that can be achieved without the need of an expensive and bulky vacuum system in comparison to other techniques such as lithography. Further, the implementation of periodic surface structures has several potential applications. The fact that the periodicity of generated LIPSS is equal to or much less than the light wavelength, therefore such structures can efficiently act as a diffraction grating. LIPSS can be explored as an advanced diffraction grating that is generated with higher degrees of freedom, hence application specific. The diffraction gratings have been commonly used as a dispersive optical element

where the dispersion can be controlled by the groove width and to create structural color which is an essential element in optical imaging such as surface-enhanced Raman spectroscopy (SERS) [62].

Further, nano-structures generated by coherent superposition of two vector vortex beams as presented in chapter 4 are of potential interest in modeling the controlled fabrication of unconventional, asymmetric surface structures. Work related to the superposition beams can be further explored and extended to study various properties of periodic structures with multiple localized regions such as 3-petal flower-like structures, for example such structures will exhibit different degrees of birefringence as each localized region compromises of different orientation of periodic nano-structures within the region. Further experiments can be devised to study the effects of such structures on incident optical vortex beams with unconventional polarization states such as spiral, radial, etc., thereby studying the interference pattern to study the role of such periodic structures in polarization selective transmission devices, and to further confine these periodic grating-like nano-structures.

In addition, nitrogen-vacancy (NV) center in diamond has emerged as a promising candidate to quantum computing and sensing implementations due to the electron spin properties of NV center and its ability to be optically read out, found and manipulated. For example, an integrated diamond photonics platform would be efficient for high-resolution magnetometry with NV centers. The long coherence time at room temperature and atomic size of NV centers allow achieving both high sensitivity of magnetic field and nanoscale spatial resolution in ambient conditions. Femtosecond laser writing technique could be used to fabricate NV color center inside the diamond. Forming micro-structures inside the diamond along with the single-photon source (NV) could be obtained via femtosecond laser writing technique and subsequent annealing. Employing fs laser beam in diamond would form vacancies, and subsequent annealing will lead to place the vacancies with a nitrogen

atom together to create NV color centers.

Bibliography

[1] L. Novotny, M. Beversluis, K. Youngworth, and T. Brown. Longitudinal field modes probed by single molecules. *Physical review letters*, 86:5251–4, 07 2001.

[2] *The Element Six CVD Diamond Handbook*. De Beers Group of Companies, 1st edition, 2017.

[3] M. Shinoda, R. Gattass, and E. Mazur. Femtosecond laser-induced formation of nanometer-width grooves on synthetic single-crystal diamond surfaces. *Journal of Applied Physics*, 105(5), 2009.

[4] L. Childress and R. Hanson. Diamond nv centers for quantum computing and quantum networks. *MRS Bulletin*, 38(2):134–138, 2013.

[5] T. A. Kennedy, J. S. Colton, J. E. Butler, R. C. Linares, and P. J. Doering. Long coherence times at 300 k for nitrogen-vacancy center spins in diamond grown by chemical vapor deposition. *Applied Physics Letters*, 83(20):4190–4192, 2003.

[6] J. P. Hadden, V. Bharadwaj, B. Sotillo, S. Rampini, R. Osellame, J. D. Witmer, H. Jayakumar, T. T. Fernandez, A. Chiappini, C. Armellini, M. Ferrari, R. Ramponi, P. E. Barclay, and S. M. Eaton. Integrated waveguides and deterministically positioned nitrogen vacancy centers in diamond created by femtosecond laser writing. *Optics letters*, 43(15):3586–3589, 2018.

[7] R. Buividas, M. Mikutis, G. Gervinskas, D. Day, G. Slekys, and S. Juodkazis. Femtosecond laser drilling of optical fibers for sensing in microuidic applications. *Proceedings of SPIE - The International Society for Optical Engineering*, 8463, 10 2012.

[8] Y. Liao, Y. Shen, L. Qiao, D. Chen, Y. Cheng, K. Sugioka, and K. Midorikawa. Femtosecond laser nanostructuring in porous glass with sub-50 nm feature sizes. *Optics letters*, 38(2):187–189, 2013.

[9] Z. Feng, J. Li, X. Qiao, L. Li, H. Yang, and M. Hu. A thermally annealed mach-zehnder interferometer for high temperature measurement. *Sensors (Basel, Switzerland)*, 14(8):14210–14221, 2014.

[10] K. Goya, M. Shiraishi, Y. Fuchiwaki, K. Watanabe, and T. Ooie. Femtosecond laser-induced surface modification and its application. In *Applications of Laser Ablation*, chapter 14. IntechOpen, 2016.

[11] M. Barberoglou, V. Zorba, E. Stratakis, E. Spanakis, P. Tzanetakis, S.H. Anastasiadis, and C. Fotakis. Bio-inspired water repellent surfaces produced by ultrafast laser structuring of silicon. *Applied Surface Science*, 255(10):5425–5429, 2009.

[12] J. Hiller, J. D. Mendelsohn, and M. F. Rubner. Reversibly erasable nanoporous anti-reflection coatings from polyelectrolyte multilayers. *Nature Materials*, 1(1):59, 2002.

[13] J. Eichstädt, G.R.B.E. Römer, and A.J. Huis in't Veld. Towards friction control using laser-induced periodic surface structures. *Physics Procedia*, 12(2):7–15, 2011.

[14] A. Y. Vorobyev and C. Guo. Enhanced absorptance of gold following multipulse femtosecond laser ablation. *Physical Review B*, 72(19), 2005.

[15] M. Mangirdas, Z. Albertas, H. Satoshi, H. Yoshio, M. Vygantas, B. Ricardas, and J. Saulius. Ultrafast laser processing of materials: from science to industry,. *Light Science & Applications*, 5(8):e16133, 2016.

[16] K. Sugioka and Y. Cheng. Femtosecond laser three-dimensional micro- and nanofabrication. *Applied Physics Reviews*, 1(4):041303, 2014.

[17] R. R. Gattass and E. Mazur. Femtosecond laser micromachining in transparent materials. *Nature Photonics*, 2(4):219–225, 2008.

[18] B.C Stuart, M.D Feit, S Herman, A.M Rubenchik, B.W Shore, and M.D Perry. Nanosecond-to-femtosecond laser-induced breakdown in dielectrics. *Physical Review, B: Condensed Matter*, 53(4), 1996.

[19] K. Sugioka and Y. Cheng. Femtosecond laser processing for optofluidic fabrication. *Lab on a Chip*, 12(19):3576–3589, 2012.

[20] S. J. Mihailov, D. Grobnic, C. Hnatovsky, R. B. Walker, P. Lu, D. Coulas, and H. Ding. Extreme environment sensing using femtosecond laser-inscribed fiber bragg gratings,. *Sensors (Basel, Switzerland)*, 17(12), 2017.

[21] S. Vukelić, P. Kongsuwan, and Y. Lawrence Yao. Ultrafast laser induced structural modification of fused silica—part i: Feature formation mechanisms. *Journal of Manufacturing Science and Engineering*, 132(6):061012, 2010.

[22] L.V. Keldysh. Ionization in the field of a strong electromagnetic wave. *Zh. Eksperim. i Teor. Fiz.*, 20(5):1945–1957.

[23] C. B. Schaffer, A. Brodeur, and E. Mazur. Laser-induced breakdown and damage in bulk transparent materials induced by tightly focused femtosecond laser pulses,. *Measurement Science and Technology*, 12(11):1784–1794, 2001.

[24] Vladimir S. Popov. Tunnel and multiphoton ionization of atoms and ions in a strong laser field (keldysh theory). *Physics-Uspekhi*, 47(9):855–885, 2004.

[25] M. Ams, G. D. Marshall, P. Dekker, M. Dubov, V. K. Mezentsev, I. Bennion, and M. J. Withford. Investigation of ultrafast laser–photonic material interactions: Challenges for directly written glass photonics. *IEEE Journal of Selected Topics in Quantum Electronics*, 14(5):1370–1381, 2008.

[26] Shane M. Eaton, G. Cerullo, and R. Osellame. *Femtosecond Laser Micromachining: Photonic and Microfluidic Devices in Transparent Materials*. Springer, 2012.

[27] K. M. Davis, K. Miura, N. Sugimoto, and K. Hirao. Writing waveguides in glass with a femtosecond laser. *Optics letters*, 21(21):1729–1731, 1996.

[28] Sivanandan S. Harilal, Justin R. Freeman, Prasoon K. Diwakar, and A. Hassanein. *Femtosecond Laser Ablation: Fundamentals and Applications*. Springer Berlin Heidelberg, 2014.

[29] J. Haverkamp, R. M. Mayo, M. A. Bourham, J. Narayan, C. Jin, and G. Duscher. Plasma plume characteristics and properties of pulsed laser deposited diamond-like carbon films. *Journal of Applied Physics*, 93(6):3627–3634, 2003.

[30] Y. L. Yao, H. Chen, and W. Zhang. Time scale effects in laser material removal: a review. *The International Journal of Advanced Manufacturing Technology*, 26(5):598–608, 2005.

[31] B. N. Chichkov, C. Momma, S. Nolte, F. von Alvensleben, and A. Tünnermann. Femtosecond, picosecond and nanosecond laser ablation of solids. *Applied Physics A: Materials Science and Processing*, 63(2):109, 1996.

[32] J. Yong, F. B. Michael, and M. W. Rodger. Laser-induced damage on single-crystal metal surfaces. *J. Opt. Soc. Am. B*, 5(3):648–659, Mar 1988.

[33] J. JJ Nivas, S. He, A. Rubano, A. Vecchione, D. Paparo, L. Marrucci, R. Bruzzese, and S. Amoruso. Direct femtosecond laser surface structuring with optical vortex beams generated by a q-plate. *Scientific Reports*, 5:17929, 2015.

[34] F. Di Niso, C. Gaudiuso, T. Sibillano, F. P. Mezzapesa, A. Ancona, and P. M. Lugara. Role of heat accumulation on the incubation effect in multi-shot laser ablation of stainless steel at high repetition rates. *Optics express*, 22(10):12200–12210, 2014.

[35] M. Shinoda, R. Gattass, and E. Mazur. Femtosecond laser-induced formation of nanometer-width grooves on synthetic single-crystal diamond surfaces. *Journal of Applied Physics*, 105(5):053102 – 053102, 2009.

[36] M. D. Shirk, P. A. Molian, and A. P. Malshe. Ultrashort pulsed laser ablation of diamond. *Journal Of Laser Applications*, 10(2):64–70, 1998.

[37] S. He, M. Hu, and C. Wang. Nano spiral stripes formation on diamond surface employing a high repetition rate femtosecond laser. In *Asia Communications*

and Photonics Conference 2013, page AF2B.24. Optical Society of America, 2013.

[38] Brian J Roxworthy and Kimani C Toussaint. Optical trapping with π- phase cylindrical vector beams. *New Journal of Physics*, 12(7):073012, 2010.

[39] Stefan W. Hell and Jan Wichmann. Breaking the diffraction resolution limit by stimulated emission: stimulated-emission-depletion fluorescence microscopy,. *Optics letters*, 19(11):780–782, 1994.

[40] R. Dorn, S. Quabis, and G. Leuchs. Sharper focus for a radially polarized light beam,. *Physical review letters*, 91(23):233901, 2003.

[41] Alan E Willner, Guodong Xie, Long Li, Yongxiong Ren, Yan Yan, Nisar Ahmed, Zhe Zhao, Zhe Wang, Cong Liu, Asher J Willner, Nima Ashrafi, Solyman Ashrafi, Moshe Tur, and Andreas F Molisch. Design challenges and guidelines for free-space optical communication links using orbital-angular-momentum multiplexing of multiple beams. *Journal of Optics*, 18(7):074014, jun 2016.

[42] V. DAmbrosio, F. Baccari, S. Slussarenko, L. Marrucci, and F. Sciarrino. Arbitrary, direct and deterministic manipulation of vector beams via electrically-tuned q-plates. *Scientific Reports*, 5(1), 2015.

[43] L. Allen, M. W. Beijersbergen, R. J. C. Spreeuw, and J. P. Woerdman. Orbital angular momentum of light and the transformation of laguerre-gaussian laser modes,. *Physical review. A, Atomic, molecular, and optical physics*, 45(11):8185–8189, 1992.

[44] P. Schemmel, G. Pisano, and B. Maffei. Modular spiral phase plate design for orbital angular momentum generation at millimetre wavelengths. *Optics express*, 22(12):14712–14726, 2014.

[45] Miles J. Padgett. Optical vortices, angular momentum, and heisenberg's uncertainty relationship. *Proc. of SPIE*, 5508, 2004.

[46] L. Marrucci, E. Karimi, S. Slussarenko, B. Piccirillo, E. Santamato, E. Nagali, and F. Sciarrino. Spin-to-orbital optical angular momentum conversion in liquid crystal "q-plates": Classical and quantum applications,. *Molecular Crystals and Liquid Crystals*, 561(1):48–56, 2012.

[47] M. Alameer, A. Jain, M. G. Rahimian, H. Larocque, P. B. Corkum, E. Karimi, and V. R. Bhardwaj. Mapping complex polarization states of light on a solid,. *Opt. Lett.*, 43(23):5757–5760, 2018.

[48] Ivan D. Rukhlenko, C. Dissanayake, and M. Premaratne. Visualization of electromagnetic-wave polarization evolution using the poincaré sphere. *Optics letters*, 35(13):2221–2223, 2010.

[49] G. B. Malykin. Use of the poincare sphere in polarization optics and classical and quantum mechanics. review. *Radiophysics and Quantum Electronics*, 40(3):175–195, 1997.

[50] Zhi-Cheng Ren, Ling-Jun Kong, Si-Min Li, Sheng-Xia Qian, Yongnan Li, Chenghou Tu, and Hui-Tian Wang. Generalized poincaré sphere. *Optics express*, 23(20):26586–26595, 2015.

[51] F. Cardano, E. Karimi, S. Slussarenko, L. Marrucci, Corrado de Lisio, and E. Santamato. Polarization pattern of vector vortex beams generated by q-plates with different topological charges. *Applied optics*, 51(10):C1–C6, 2012.

[52] Donna Strickland and Gerard Mourou. Compression of amplified chirped optical pulses. *Optics Communications*, 56(3):219–221, 1985.

[53] C. Rullière. *Femtosecond Laser Pulses*. Springer New York, 2005.

[54] J. JJ Nivas, S. He, Z. Song, A. Rubano, A. Vecchione, D. Paparo, L. Marrucci, R. Bruzzese, and S. Amoruso. Femtosecond laser surface structuring of silicon with gaussian and optical vortex beams,. *Applied Surface Science*, 418:565–571, 2017.

[55] E. Hecht. *Optics*. Addison-Wesley, San Francisco, CA, 4th edition.

[56] E. Allahyari, J. JJ Nivas, F. Cardano, R. Bruzzese, R. Fittipaldi, L. Marrucci, D. Paparo, A. Rubano, A. Vecchione, and S. Amoruso. Simple method for the characterization of intense laguerre-gauss vector vortex beams,. *Applied Physics Letters*, 112(21):211103, 2018.

[57] J. Bonse, J. Krüger, S. Höhm, and A. Rosenfeld. Femtosecond laser-induced periodic surface structures. *Journal of Laser Applications*, 24, 2012.

[58] Y. Jin, O. J. Allegre, W. Perrie, K. Abrams, J. Ouyang, E. Fearon, S. P. Edwardson, and G. Dearden. Dynamic modulation of spatially structured polarization fields for real-time control of ultrafast laser-material interactions. *Optics express*, 21(21):25333–25343, 2013.

[59] Y. Shimotsuma, P. G. Kazansky, J. Qiu, and K. Hirao. Self-organized nanogratings in glass irradiated by ultrashort light pulses,. *Physical review letters*, 91(24):247405–247405, 2003.

[60] V. R. Bhardwaj, E. Simova, P. P. Rajeev, C. Hnatovsky, R. S. Taylor, D. M. Rayner, and P. B. Corkum. Optically produced arrays of planar nanostructures inside fused silica,. *Physical review letters*, 96(5):057404–057404, 2006.

[61] D. Ramanathan and Pal A. Molian. Micro- and sub-micromachining of type iia single crystal diamond using a ti:sapphire femtosecond laser,. *Journal of Manufacturing Science and Engineering*, 124(2):389–396, 2002.

[62] Bin-Bin Xu, Zhuo-Chen Ma, L. Wang, R. Zhang, Li-Gang Niu, Z. Yang, Yong-Lai Zhang, Wan-Hua Zheng, B. Zhao, Y. Xu, Qi-Dai Chen, H. Xia, and Hong-Bo Sun. Localized flexible integration of high-efficiency surface enhanced raman scattering (sers) monitors into microfluidic channels. *Lab on a Chip*, 11(19):3347–3351, 2011.